Title
Energy Recycling and Management for Lower Limb Exoskeleton

Author
Lee, Hao

Publication Date
2023

UNIVERSITY OF CALIFORNIA
Los Angeles

Energy Recycling and Management for Lower Limb Exoskeleton

A dissertation submitted in partial satisfaction
of the requirements for the degree
Doctor of Philosophy in Mechanical Engineering

by

Hao Lee

2023

ABSTRACT OF THE DISSERTATION

Energy Recycling and Management for Lower Limb Exoskeleton

by

Hao Lee
Doctor of Philosophy in Mechanical Engineering
University of California, Los Angeles, 2023
Professor Jacob Rosen, Chair

Lower Limb Exoskeleton, a wearable robot that is designed to provide lower limb assistance to users, has been rapidly developed in the previous decade. The goal of these robots is to replace human labor with robots while still having humans involved. However, while these robot suits provide sufficient assistance to the users, the efficiency of the robot is often overseen. Thus, restrict the exoskeleton's operating time or required it to connect to an external power supply. However, there is plenty of energy wasted in human motions. In this study, we target ”loaded bipedal walking” as the primary motion to assist.

In chapter 2, we applied trajectory optimization on different mechanical designs for lower-limb exoskeletons. It is commonly known that humans tend to use more energy to walk compared to other limb-based locomotion animals. This higher energy usage is due to ”heel strikes” and ”negative work” during human gait. Passive walkers elevate this phenomenon by utilizing elastic joints that absorb/reuse some of the negative work. The objective of this study is to absorb energy at one phase of the gait cycle, store it, and then release it at a later phase through the use of a lower limb exoskeleton. Knee geometry is one important factor in energy efficiency during gait. Animals with reversed knees compared to humans (backward

knee), such as ostriches, exhibit improved energy efficiency. As part of this study, new energy optimization strategies were developed utilizing collision-based ground reaction forces and a discrete lagrangian. The minimal cost of transport (CoT) gait patterns were calculated with both forward-knee and backward-knee human-exoskeleton models. Simulation results show that wearing a backward-knee exoskeleton can reduce the CoT by 15% of while carrying external loads ranging from 20 to 60 kg. In addition, when the exoskeleton utilized energy recycling, the CoT was shown to be further reduced to 35%. These simulation results suggested that the optimal design for an exoskeleton aimed at utilizing energy recycling principles should incorporate backward-knee configurations much like those found in energy-efficient biped/quadruped animals. In fact, since the potential energy sources (heel strikes, negative work) and the main energy consumer (ankle push-off) occurs in the opposite legs, the ideal actuators for the exoskeleton need to be able to recycle, store, and transfer energy between different legs.

To satisfy the actuator's requirements from chapter 2, in chapter 3 we choose pneumatic actuators as the actuator for our exoskeleton. Pneumatic actuators are a popular choice for wearable robotics due to their high force-to-weight ratio and natural compliance, which allows them to absorb and reuse wasted energy during movement. However, traditional pneumatic control is energy inefficient and difficult to precisely control due to nonlinear dynamics, latency, and the challenge of quantifying mechanical properties. To address these issues, In chapter 3, we developed a wearable pneumatic actuator with energy recycling capabilities and applied the sparse identification of nonlinear dynamics (SINDy) algorithm to generate a nonlinear delayed differential model from simple pressure measurements. Using only basic knowledge of thermal dynamics, SINDy was able to train models of solenoid valve-based pneumatic systems with a training accuracy of 90.58% and a test accuracy of 86.44%. The generated model, when integrated with model predictive control (MPC), resulted in a 5% error in pressure control. By using MPC for human assistive impedance control, the actuator was able to output the desired force profile and recycle around 88% of the energy

used in negative work. These results demonstrate an energy-efficient and easily calibrated actuation scheme for designing assistive devices such as exoskeletons and orthoses.

In chapter 4, we presented Pneumatic Exoskeleton with Reversible Knee (PERK). It utilizes the pneumatic actuators we developed in chapter 3, and the control strategies we concluded in chapter 2. Three clinical trials were done on three different test subjects. The results showed despite different walking patterns across different test subjects, there is less potential energy change during the swing phase of walking, potentially reducing the energy loss during the heel strike. In addition, during the double support phase, there is less energy consumption in the pneumatic system while configuring it as backward-knee, indicating it is easier or more intuitive for the user to have the exoskeleton recycling the dissipated energy with the backward-knee mechanism.

The dissertation of Hao Lee is approved.

Tyler Roy Clites

Tetsuya Iwasaki

Jason L. Speyer

Jacob Rosen, Committee Chair

University of California, Los Angeles

2023

To all those who supported me along the way...

TABLE OF CONTENTS

LIST OF FIGURES

LIST OF TABLES

Acronyms

COM *Center of Mass.*

COP *Center of Pressure.*

CoT *Cost of Transportation.*

MPC *Model Predictive Control.*

SINDy *Sparse Identification of Nonlinear Dynamics.*

ACKNOWLEDGMENTS

This arduous journey has far surpassed my initial expectations. Throughout my graduate studies, unanticipated challenges and unprecedented global crises presented additional hurdles that have left me uncertain whether I would still possess the fortitude to make the same choices. Thankfully, I have not traversed this path alone. It is with utmost gratitude and appreciation that I acknowledge all those who have contributed to the completion of this degree.

I extend my sincerest thanks to my advisor, Professor Jacob Rosen, for his invaluable guidance and unwavering support. From the outset, he welcomed me into his lab and provided mentorship throughout my years at UCLA.

To the members of my committee, I am profoundly grateful for your wisdom and benevolence. Dr. Speyer and Dr. Iwasaki, despite not being under your direct tutelage, you generously dedicated your valuable time to respond to my inquiries and offer feedback on my sometimes naïve ideas. Dr. Clites, your critical suggestions proved instrumental, and I regret not having had the privilege of knowing you earlier in my studies.

To my fellow lab mates, I consider myself truly fortunate to have collaborated with each and every one of you. Jianwei, you have been an exceptional guide, akin to a second advisor. Your expertise and commitment to refining engineering intricacies consistently astound me. Without your input, my studies would have lacked functionality. Changyeob, our friendship has been an invaluable source of motivation. The time we spent attending classes together remains a cherished memory. Peter, our banter has provided delightful moments akin to the proverbial cherry atop a cake. Erik, your humor helped dispel self-doubt during challenging times. Seungmin and Mianzhi, the support and camaraderie we shared during the most arduous periods were truly invaluable. Marshall and Sardor, my esteemed undergraduate assistants, your unwavering dedication and tireless efforts, even on weekends, were crucial to the success of my experiments. I only wish I could offer as much guidance as you have

provided me. Lastly, to Bita, Yasmin, and Leonardo, I am grateful for your unwavering support and cherished friendship.

To Nicole, I extend my heartfelt thanks for being an exceptionally patient and encouraging confidant. Your unwavering support and the solace you provide during my moments of childish lamentation and sorrow have been immeasurable. Your faith and optimism have kept me steadfastly focused on my goals.

Finally, to my family—Mom, Dad, Grandma, Tian, and Ying—I owe an immeasurable debt of gratitude. Without each of your unwavering support, I would not have reached this point. Thank you for shouldering my familial responsibilities while I selfishly pursued my dreams. I wish there were a way to compensate for my absence. I love you all.

VITA

2009-2013	B.S. in Mechanical Engineering, National Chiao Tung University.
2015-2023	Ph.D. Candidate in Mechanical Engineering, UCLA.

PUBLICATIONS

H. Lee, **P. W. Ferguson**, and J. Rosen, ”Lower Limb Exoskeleton Systems—Overview,” in *Wearable Robotics: Systems and Applications*, Academic Press, 2020, pp. 1–22.

H. Lee and J. Rosen, ”Lower Limb Exoskeleton - Energy Optimization of Bipedal Walking With Energy Recycling - Modeling and Simulation,” in *IEEE Robotics and Automation Letters*, vol. 8, no. 3, pp. 1579-1586, March 2023.

CHAPTER 1

Reducing Energy Consumption in Human Walking with Exoskeletons

1.1 Human Performance Augmentation Exoskeleton

Lower Limb Exoskeleton, a wearable robot that is designed to provide lower limb assistance to the users, has been rapidly developed in the previous decade. The goal of these robots is to replace human labor with robots while still having humans involved. Compare to having humans control a robot, these wearable robot suits have the potential to operate in any place that humans can reach, while traditional robots arms require extra space or modification of the environment. Yamamoto made the first attempt by developing a full body exoskeleton that is capable of lifting 60 kg during nursing [1], [2]. However, this exoskeleton only focuses on transferring patients from beds to wheelchairs, the mobility of the exoskeleton was not considered. On top of that, only the arm, waist, and knees are actuated, resulting in extra loads on user's ankle joints. In order to address this issue, Kazerroni et al., presented a movable load-carrying, full lower-body exoskeleton- BLEEX, which is later commercialized as Ekso [3], [4]. BLEEX can achieve "transparency", which means the user has minimal interaction with the carrying load by transferring the weight of the load to the ground. Linear hydraulic actuators are selected for its high force density. Nevertheless, while these exoskeletons assist the user, it is not energy efficient. For example, the net metabolic cost reduction is not proportional to exoskeletons' assistance [5]. This may add unnecessary energy consumption thus limiting the operating time of the lower limb exoskeleton. Around

72% of the exoskeleton is driven by electric motors [6], most of them are the servo motors due to its advanced position based control system. Nevertheless, the efficiency of such systems is limited by the fundamental difference between it and human joints. For example, the range of human knee joint angular position may range from +20 Deg. to +110 Deg., and the equivalent angular velocity may be less than 30 rpm [7] but with high torque output, while most motors operate in 360 Deg. and have maximized efficiency and torque output in higher rpm. Practically, gear reduction is applied to compensate these differences. However, the dilemma of gear ratio appears, which is high gear ratio create larger torque but cannot meet the high angular acceleration in human joints. On top of that, the capacity of the batteries are often limited. For instance, a common cellphone power bank can only provide 25 W of power for an hour, while a 60 kg male may need more than 100 W for walking. Although this may be solved by having more batteries integrated on the exoskeleton, it will increase the overall weight thus reduce the amount of load it can carry, which results in a dilemma of exoskeleton's design.

Some researchers have attempted to optimize the actuating system. Alò [8] designed an transmission system between the motors and the knee joint. It contains a fly wheel with infinitely variable transmission, which is basically a continuous variable transmission with sudden reverse rotating direction ability. Since the motor could operate at a rotational speed with better energy efficiency, Alò successfully reduced the energy consumption of the motors. Albeit not equivalent to reduce overall energy consumption, the extra weight's effect is unknown.

1.2 Energy Loss and Harvesting in Bipedal Walking

On the other hand, many researchers believe there is potential to harvest energy from human motion [9], [10]. Among all potential energy sources, impact loss in ground-level walking has draw attention. Bipedal walking differentiates humans from other mammals.

The need for only two lower limbs for locomotion allowed for our upper limbs to evolve into highly dexterous manipulators with fine motor control. The cost associated with this evolutionary trajectory is a reduction in gait efficiency. The ”heel strike” (the point in time during the gait cycle where the heel first contacts the walking surface), and the negative work to ”slow-down” human limbs” are considered the major causes of energy loss in the human gait cycle [11], [12]. Bipedal walking can be viewed as a cycle of intentional forward falling halted by collision between the stepping leg and the walking surface. As with any inelastic collision there is an inherent loss of energy to the environment. Devices based on harvesting electrical energy from these losses are discussed in [13]–[18]. The primary issue with this approach is that the metabolic cost associated with wearing the device greatly exceeds their generated electrical power. Thus, rather than converting mechanical energy into electrical energy, studies such as [19] have shown benefits in directly storing the energy mechanically. In fact, such a concept has already been utilized during evolution. Evidence suggests that not all energy is lost in heel-strike collisions. Tendons, acting as spring-like passive structures, absorb and store some kinetic energy [20]. Malcom [21] showed that energy recovery can be improved by increasing the extension of the Achilles tendons by assisting the rear ankle just before heel strike can improve walking efficiency. These concepts have motivated similar approaches with robotic devices [22]–[24]. State-of-the-art devices based on this concept are inspired by the human body and utilize tendon-like serial elastic components for harvesting, storing, and reusing energy [25]–[27].

It is noteworthy that human motion-enhancing devices typically do not include full-lower-body exoskeletons, which encompass the thighs, calves, and feet. The reason for this is that the energy required to walk with the device increases proportionally with the mass of the additional load and its distance from the individual’s center of mass [28]. To optimize energy efficiency, researchers frequently minimize the weight added to the distal limbs by including solely the actuator and have the load carried at the user’s back [29]. However, this configuration requires the user’s body to serve as the ”mechanical frame” that supports the load, which restricts the amount of weight that can be carried due to the physical limitations of the human body.

1.3 Forward-knee and Backward-knee of Bipedal Walking

However, the human body should restrict designing the exoskeleton. In fact, two primary leg structures have evolved for bipedal locomotion: forward-knee and backward-knee. The forward-knee configuration, observed in humans and other primates, involves the knee joint pointing toward the direction of the gait. The backward-knee configuration, observed in birds such as ostriches, involves the knee joint pointing against the direction of the gait. In humans, the forward-knee configuration allows for the recycling of expended energy from heel strike using the Achilles tendons [30], [31]. During the single support phase of walking, the support leg's Achilles tendon recoils and stores rotational kinetic energy as elastic energy. This energy is then released during toe-off via ankle plantarflexion, propelling the leg forward [30], [32]. However, this innate mechanism of energy recycling is not fully utilized during walking, as previous studies have demonstrated that energy storage and expenditure via tendon stretching and relaxing is only fully optimized during running [33]–[35]. Therefore, while the forward-knee configuration has some limitations in terms of optimizing energy consumption during walking, it does not restrict the design of exoskeletons.

Previous studies indicate that running efficiency for the backward-knee configuration is superior due to several factors. One of these is the extensive use of tendons elasticity. Rubenson [36] showed that the storage and subsequent reuse of elastic energy is 120% higher in ostriches than in humans. Another factor is how serial elastic elements (tendons) cross in the two types of knees. Rankin [37] showed that ostriches, which have tendons that cross both the knee and hip, experienced greatly reduced torque in the hip joints, when compared to forward-knee animals [33]. Additionally, the backward-knee configuration does not require extra hip motion to compensate for knee retraction, a trait present in forward-

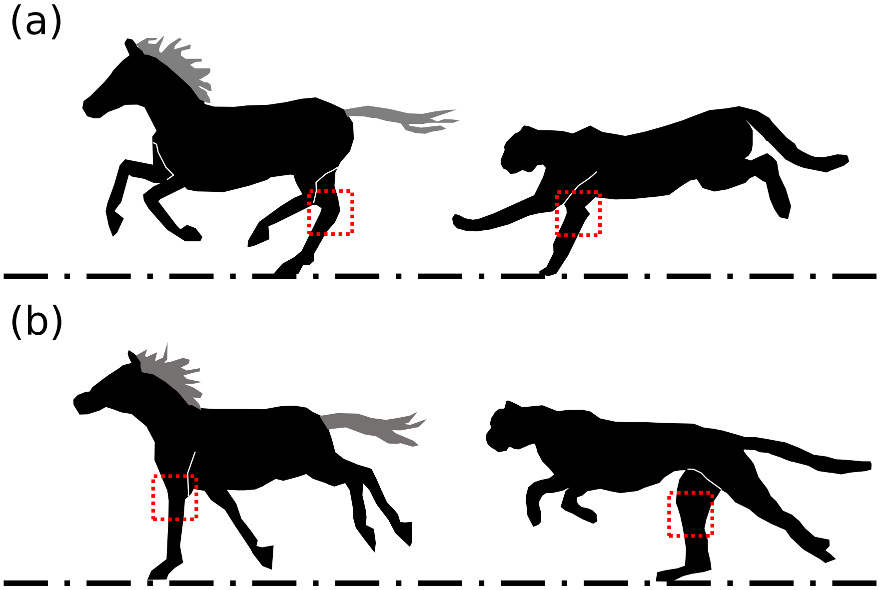

Figure 1.1: How quadrupedal animals utilize different knee configurations: (a) absorb impact with backward-knee configuration (b) Propel with forward-knee configuration

knee walking [38]. The backward-knee configuration also allows for better support of body weight by lowering metabolic rate, as evident in Guinea fowls [39]. All these potential advantages motivate the question: can energy efficiency be increased for humans by adopting a backward-knee configuration?

Unfortunately, Flynn [40] demonstrated that walking or running backward does not enhance energy efficiency for humans, indicating that the forward-knee configuration is optimal for human walking. However, a potential solution could be a hybrid configuration. Quadrupedal animals, unlike bipedal animals, employ both forward-knee and backward-knee configurations. For example, the front and rear legs of horses or felines have opposite knee-bending directions (Fig. 1.1). Although the galloping gait of horses differs from that of felines [41], both absorb impact with backward-knees and use forward-knees for ankle push-off. This suggests that backward-knees have superior impact absorption, while forward-knees are more energy-efficient for propulsion. Therefore, integrating a backward-knee exoskeleton with the biological forward-knee configuration of humans has the potential to significantly enhance overall locomotion efficiency.

1.4 Inter Limb Energy Transferring

In recent years, there has been a growing interest in enhancing human walking efficiency through the design of exoskeleton systems. However, improving a mechanism that has evolved for millions of years is challenging. Traditional approaches to reducing walking energy consumption, such as the addition of springs to increase the stiffness of the Achilles tendon, have been limited by their reliance on the muscle-skeleton properties of the human body. As a result, these "add-ons" only allow for the recovery and reuse of mechanical energy in the same joint, which is not ideal for bipedal walking. In fact, it may cause unwanted resistance in other joints. For instance, Uchiada [34] showed that even assistance provided by ideal actuators during running is still transferred to joints as unwanted resistance. Dembia [42] showed that due to the coupling of muscles in the leg, torques that assist the knee can also increase the resistive torque at the hip joints. In addition to these unintentional resistances, the provided assistance and weight of a wearable device can affect the mechanics of bipedal walking, leading to suboptimal gait patterns [28]. Besides joint coupling, another challenge in improving the energy efficiency of walking is the asynchronism between the impact loss that occurs when the leading leg contacts the ground and the main effort of moving forward, which is the ankle push-off from the rear leg. While storage devices can be used to temporarily store energy, the energy loss during conversion is not negligible. However, these restrictions do not apply to robotics systems, which can transfer energy from one leg to another mechanically.

Zhang [43] proposed a design for an exoskeleton system that connects the ankles of the user via springs and pulleys, reducing the mechanical work of the tailing ankle during walking by transferring the negative work of dorsiflexion from the leading foot. However, while this design reduced the overall mechanical work of the tailing ankle, it also resulted in an increase in overall energy consumption due to the fact that the dorsiflexion of the leading foot is not the "impact loss", but rather negative work that will be absorbed by the Achilles tendon and later reused for ankle push-off. To address these limitations, future research should focus on developing exoskeleton systems that can utilize the impact loss of the leading leg and reuse it on the following leg.

1.5 Study Contribution

In this study, we will focus on improving the energy efficiency of the full lower-limb exoskeleton. The goal of this study is to provide the guidelines of optimizing the design of load-carrying exoskeletons that can be used in the industry. The study will be divided into three sections. In chapter 2, we will use numerical optimization on models with exoskeletons in different knee-bending directions to determine the superior mechanical design. To reduce the energy consumption of the actuators, in chapter 3 we proposed the pneumatic actuator that can reuse the energy of generating negative work on positive work. A novel data-driven control method is proposed and verified in the same chapter. Lastly, in chapter 4, we constructed a full lower-body pneumatic exoskeleton that can be configured as both forward and backward knee bending directions that integrated with our novel pneumatic actuators to verify the conclusions that we learned in chapter 2 in a real-world scenario.

CHAPTER 2

Optimal Assisting Strategies for Exoskeleton - Simulation

2.1 Introduction

In this chapter, trajectory optimization is employed to examine the interactions between human, assistive forces, and wearable devices. There are two prevalent methods for trajectory optimization: multiple shooting and direct method [44]. The multiple shooting approach utilizes numerical integration for computing the gradient of a cost function and updating the control input accordingly. Although it ensures the trajectories is physically feasible, it is computationally expensive and frequently fails to satisfy path constraints, such as achieving a specific endpoint. In contrast, the direct method, also called the direct collocation method, defined both system states and control inputs as independent variables, leading to simplified dynamics of the model presented as nonlinear constraints throughout each time step. One such example is represented by the formula $x'(t)\Delta t = x(t + \Delta t) - x(t)$. The direct method generally demonstrates higher efficiency and improved convergence when compared to the multiple shooting method. Kelly [45] demonstrated the use of the direct method in generating trajectories for bipedal models.

To generate ground reaction forces (GRF), we include a contact-based GRF into our optimization. The modeling of ground reaction forces (GRF) is crucial for the simulation of human gait. The direct method of modeling GRF oversimplifies the process, as it views forces and states as independent variables, which cannot adequately model GRF since it is correlated with current joint angles and velocities. To overcome this limitation, recent studies have modeled GRF as impulses that act only during heel strike [46], [47]. Nevertheless, this approach neglects the crucial heel-toe walking pattern [48] and causes the foot to just bounce off the ground. To address this issue, a two-layer optimization method called Contact Invariant Optimization has been proposed [49]. It consists a two-layer optimization, with a nonlinear optimization as the outer layer, and a convex quadratic program as the inner layer. The inner layer solves the joint torques and the GRF with a nominal joint trajectory, while the outer layer solves the joint trajectories with the path constraints. Though it has been proven to generate contact forces in multiple scenarios, it is computationally expensive. In our optimization, we categorize GRF into collision-related and steady forces. Nonlinear models are used to consider the compliance of the foot for collision-related GRF [50]–[52]. To reduce the computational cost, the dynamics are discretized with a variational integrator is used [53]. This approach has been shown to generate contact forces in multiple scenarios. Details of these methods will be elaborated in the following section.

2.2 Model Generating

Three types of models are used in the optimization: a solo human, a human wearing a forward-knee exoskeleton, and a human wearing backward-knee exoskeleton (Fig. 2.1). Each model carries a load near the center of mass (COM) of the torso to minimize the energy consumption since it is proportional to its distance from the COM [28]. The assumption is made since we believe humans will adjust the load's location to have the minimum effect on the metabolic rate. The length, mass, and inertia of each segments are referenced from Winter [54] (Table 2.1, Fig. 2.2). The physical parameters of the exoskeleton are referenced from the lower limb exoskeleton at *Bionics Lab, UCLA* (Fig. 2.3). The parameters of the exoskeleton are shown in table 2.2.

As shown in Fig. 2.1, human models consist of six links and human exoskeleton hybrid

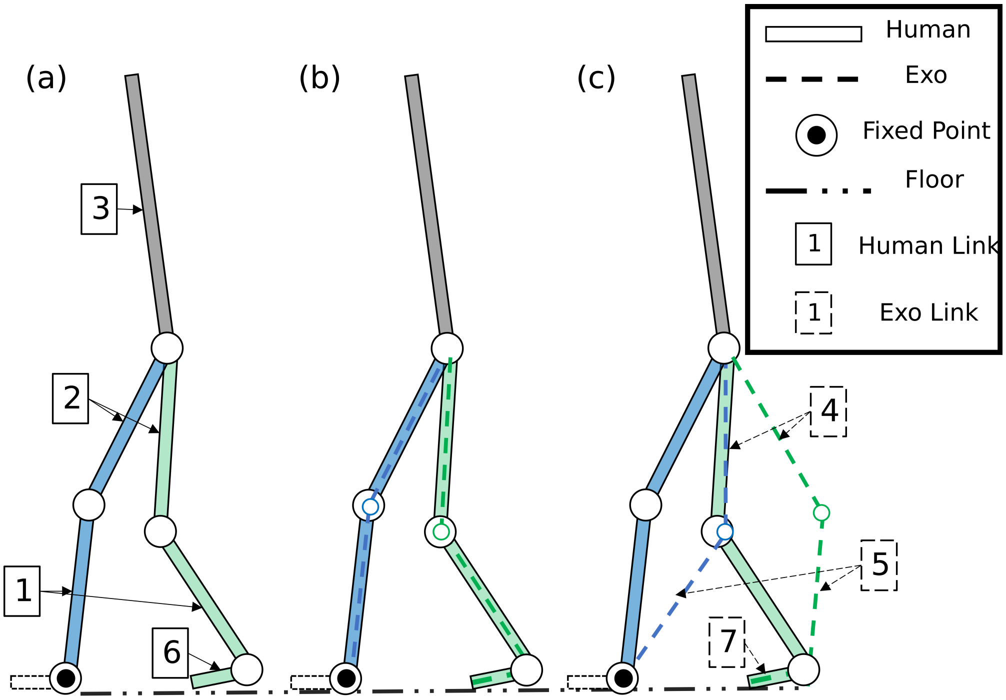

Figure 2.1: (a) Model without the exoskeleton. (b) Model with forward-knee exoskeleton. (c) Model with backward-knee exoskeleton.

models consist of ten links. All the links are connected with revolute joints. The elasticity of muscles and tendons is simulated with nonlinear torsional springs at each revolute joint with spring constant from Arnold [55]. Additional damping coefficients are added to the human joints to simulate synovial joint friction [56].

Table 2.1: Human model's parameters. m: segment's mass. M: total body weight (human). L: segment's length. L_c: center of mass(proximal). RoG: Radius of gyration

Segment	i	m/M	L_i/H	$L_{c,i}/L_i$	RoG/L_i
Tibia	1	0.0645	0.245	0.433	0.302
Thigh	2	0.1	0.245	0.433	0.323
Torso	3	0.678	0.34	0.5681	0.496
Foot	6	0.0145	0.152	0.5	0.496
	h	—	0.039	-	-

Table 2.2: Exoskeleton model's parameters.

Segment	i	$m(kg)$	L_i/H	$L_{c,i}/L_i$	RoG/L_i
Tibia	4	1.7	0.245	0.5	0.083
Thigh	5	1.7	0.245	0.5	0.083
Foot	7	0.8	0.152	0.5	0.083
	h	–	0.039	-	-

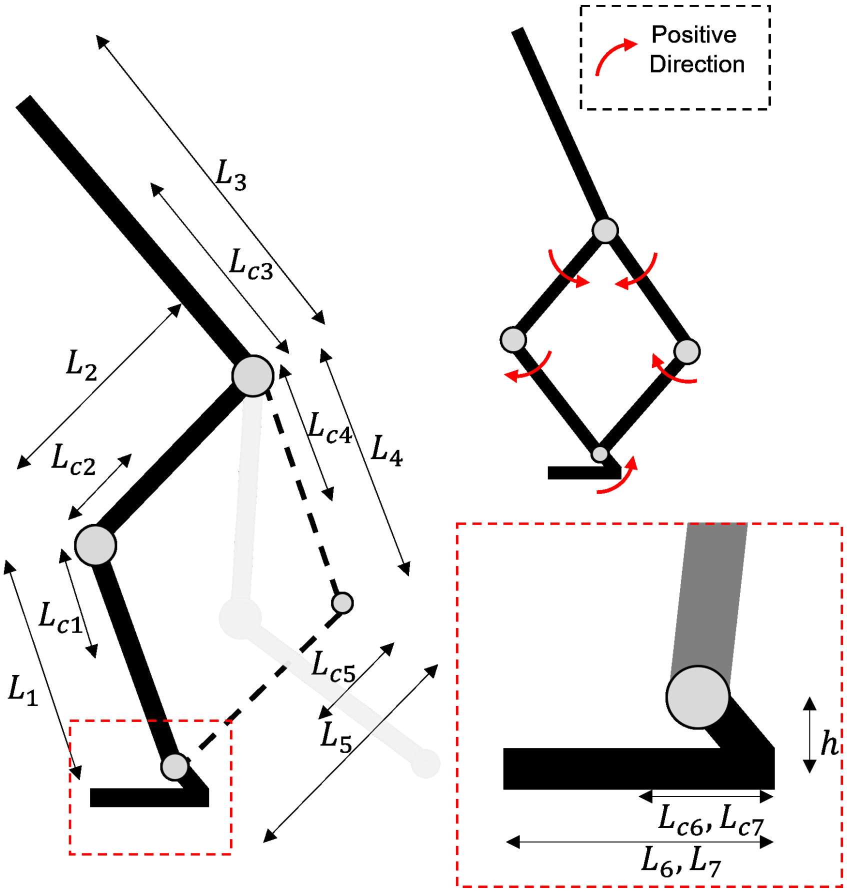

Figure 2.2: Definition of link lengths, COM positions (single leg).

2.3 Multi Phases Optimization

As mentioned in the introduction, each gait cycle is divided into different phases based on the contact conditions, and simulated with different dynamical functions accordingly. In most studies, gaits are divided into two phases: single support phase and double support

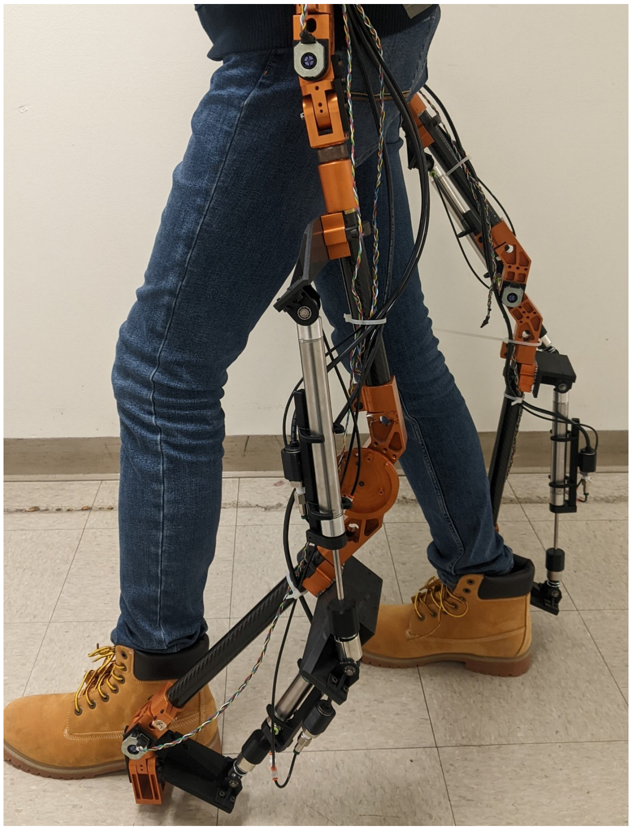

Figure 2.3: The backward-knee pneumatic exoskeleton developed in Bionics Lab, UCLA.

phase [57]. The single support phase refers to the duration in that only one leg is in contact with the ground (often called the swing phase). The double support phase, as its name suggests is the brief time when both legs have contact with the ground. Unfortunately, the two-phase method does not suit the collision-based GRF function (equation 2.2) since it can only be applied to collision-like contact such as heel strike. It fails at steady contact seen in ankle push-off. Thus, in our study, we further divide the double support phase into two sub-phases: an ankle push-off phase and a loading response phase, both of which are shown in Fig. 2.4. During the ankle push-off phase, the rear toe is always in contact with the ground. On the other hand, the GRF during the loading response phase is generated based on the toe's position and velocity. Thus, state variables in different phases should have different dimensions, which are defined in (2.1). For the ankle push-off phase (P_1), we only define the rear toe's GRF $f_{x_{toe}}, f_{y_{toe}} \in \mathbf{R}$, The duration of this phase is referenced from normal human gaits [57]. For the loading response phase (P_3), we define the horizontal GRF at the toe (f_x^{toe}) $\in \mathbf{R}$ and heel ($f_x^{heel} \in \mathbf{R}$). We did not need to explicitly define the vertical GRF like in the ankle push-off phase because it is a function of q in the loading response phase. Joint angle $q \in \mathbf{R}^n$ and joint torque $u \in \mathbf{R}^n$ are also defined in every phase. All variables are discretized in order to apply the direct collocation method.

$$\begin{aligned} q_n, u_n, f_{x_n}^{toe}, f_{y_n}^{toe} \forall n \in P_1 \\ q_n, u_n \forall n \in P_2 \\ q_n, u_n, f_{x_n}^{toe}, f_{x_n}^{heel} \forall n \in P_3 \end{aligned} \tag{2.1}$$

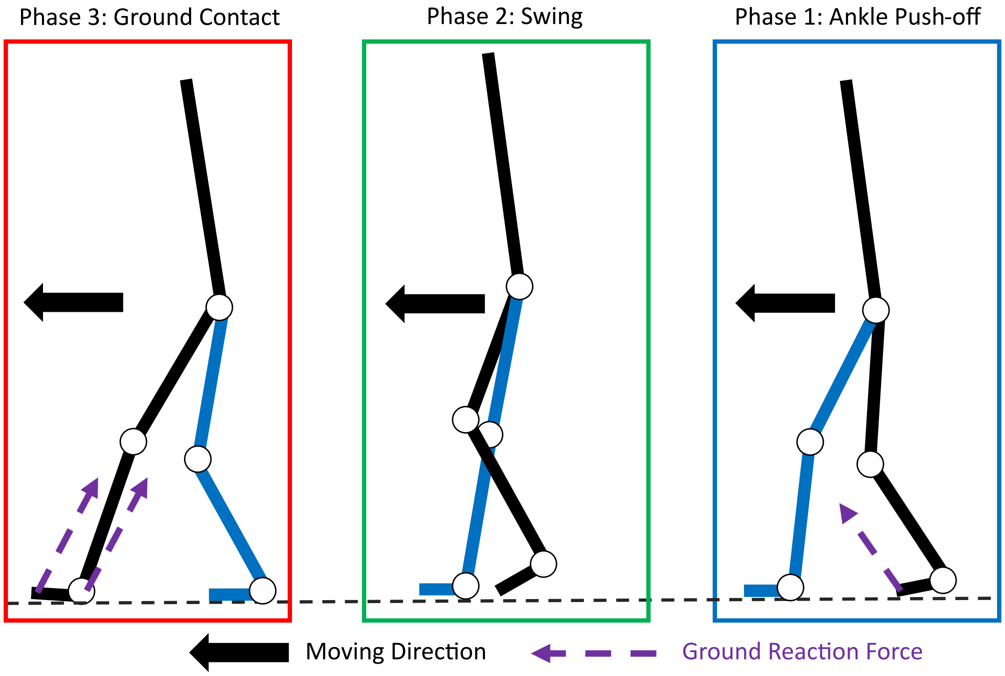

Figure 2.4: The system dynamics is divided into 3 different phases. P1: Ankle push-off phase, P2: swing Phase, P3: loading response phase.

2.4 Ground Reaction Forces

The GRF functions in the loading response phase (P_3) are listed as below (equation 2.2). The vertical GRF were defined based on Peasgood [51].

$$\begin{aligned}
F_n(q_t) &= \sigma(q_t)(ky(q_t)^2 + b(q_t)\dot{y}(q_t)) \\
b(q_t) &= c_{max}\frac{y(q_t)}{d_{max}} \\
\sigma(q_t) &= \frac{1}{1 + e^{500(y(q_t)-d_{max})}} \\
d_{max} &= 0.01, c_{max} = 4000 \\
d_{max} &= \frac{BW}{2(d_{max})^2} \\
q_t &= \frac{q_n + q_{n+1}}{2}, \dot{q}_t = \frac{q_{n+1} - q_n}{h}
\end{aligned} \tag{2.2}$$

The vertical depth that the point of contact penetrates the ground surface is designated as y, with d_{max} representing the maximum attainable penetration depth. The overall weight of the model is denoted by BW. The values of q_t and $\dot{q}t$ are derived from a discrete time series, as per Manchester [53]. The damping coefficient, b, is to increase linearly with depth, and the maximum damping coefficient, $Cmax$, is defined based on the findings of Brand et al. [58]. The spring constant, k, is formulated such that the ground reaction force equates to the total body weight at the midpoint of the double support phase. To avoid the instability that may arise due to an excessively high spring constant, we have relaxed the constraints by raising the contacting surface 10 mm above the ground, following the approach adopted by Manchester [53]. In accordance with our definitions, the majority of the body weight is transferred to the front foot during the rear foot toe-off phase.

The horizontal GRF were constrained by the friction cone, which are shown in equation 2.4.

$$f_{x_n} \leq \mu f_{y_n}, -f_{x_n} \leq \mu f_{y_n} \forall n \in P_1 \tag{2.3}$$

$$(f_{x_n})^2 \leq \mu^2 F_y(q_n)^2, \forall n \in P_3 \tag{2.4}$$

$$f_x J(q)\dot{q} \leq 0 \tag{2.5}$$

μ is the static friction coefficient, $J(q)$ is the Jacobian. Equation 2.5 constraints the direction of horizontal force must against the contacting point.

2.5 Dynamic Constraints

The dynamic constraints used in this study are similar to those defined by Manchester [53]. This approach entails expressing the Lagrangian of mechanics in discrete states, where the velocity is redefined as the difference between two positions. As a result of this process, the Lagrangian is no longer a function of position and velocity, but instead a function of positions alone. Given joint position q and joint velocity $\dot{q}$, the original Lagrange-D'Alembert principle takes the following form:

$$\delta \int_{t_0}^{t_f} \mathcal{L}(q, \dot{q}) dt + \int_{t_0}^{t_f} F(t) \delta q dt = 0 \tag{2.6}$$

By substituting the joint velocity with their difference, and position with the average between each time steps, one can form the dynamic constraints:

$$\begin{aligned} &\frac{\partial \mathcal{L}(q_{n-1}, q_n)}{\partial q_n} + \frac{\partial \mathcal{L}(q_n, q_{n+1})}{\partial q_n} \\ &+ \frac{1}{4} F(q_{n-1}) + \frac{1}{2} F(q_n) + \frac{1}{4} F(q_{n+1}) = 0 \end{aligned} \tag{2.7}$$

$$F(q_n) = u_n + J(q_n)^T F_{ext}(n) \tag{2.8}$$

$$N \triangle t = t_f \tag{2.9}$$

N is the total number of the discrete steps, and $\triangle t$ is the sampling period.

2.6 Path Constraints

To ensure continuity, both the joint positions and the joint velocities of the first and the last frame are related with an affine function:

$$q_0 = A q_N + b \tag{2.10}$$

$$u_0 = A u_N \tag{2.11}$$

To assure the ground reaction force (GRF) only occurs during the double support phase, supplementary path constraints are deemed necessary. Specifically, during the swing phase, it is imperative that both the toe and the heel remain above the ground, as dictated by Equation 2.13. Additionally, our analysis revealed that limiting the forward movement of the center of mass by constraining its horizontal velocity led to a significant improvement in convergence. These conditions may be represented mathematically as follows:

$$v_x^{hip}(q_n) \leq 0 \tag{2.12}$$

$$p_y^{toe}(q_n) \geq 0, p_y^{heel}(q_n) \geq 0, \forall n \in P_2 \tag{2.13}$$

v_x^{hip} is the horizontal velocity of the hip's center of mass, and p_y^{toe}, p_y^{heel} are the vertical position of the toe and the heel.

2.7 Optimization

The present investigation aims to determine the optimal trajectory with the minimum cost of transportation (CoT). The definition is inspired by Schultz's work [47], where it demonstrated that minimizing the norm of joint torques produced a more natural gait compared to minimizing mechanical energy. The CoT is determined through a series of steps. Firstly, the joint torque $u = \begin{bmatrix} u_0 & u_1 & \dots & u_N \end{bmatrix}$ is partitioned into two groups based on the work generated. These groups are denoted as u^{pos}, which produces only positive work, and u^{neg}, which produces only negative work. The mathematical representation of these groups is provided in equation 2.14.

$$\begin{aligned} u &= u^{pos} + u^{neg} \\ u^{pos} &\odot \omega \geq 0 \\ u^{neg} &\odot \omega < 0 \end{aligned} \tag{2.14}$$

where ω is the joints' angular velocity, and $\odot$ is the elementwise-product.

In order to incorporate the energy recycling capability of the exoskeleton, this study introduces two constant parameters: the *negative work recycling efficiency* (μ_{neg}) and the *positive work assisting efficiency* (μ_{pos}). The exoskeleton is capable of providing a portion of the torque (τ^{neg}) required to generate negative work by harvesting energy. This portion of torque generated by the exoskeleton is denoted as μ_{neg}, as shown in equation 2.15. The total negative work generated by the exoskeleton is computed as the inner product of the angular velocity (ω) and the torques it generates (τ^{neg}). However, due to energy loss during energy recycling, only a portion of the negative work can be stored, which is represented as W_{rec}. The ratio between the recycled energy and the total negative work is denoted as μ_{pos}, as it will be utilized to assist the positive work in the later phases of walking.

$$\mu_{neg} = \frac{\|\tau^{neg}\|}{\|u^{neg}\|}, \mu_{pos} = \frac{W_{rec}}{\|\omega^T \tau^{neg}\|} \tag{2.15}$$

The research has shifted the focus from mechanical work to the norm of the joint torques for determining the cost of transportation (CoT). Hence, an investigation into the role of the recycled energy (W_{rec}) in assisting the user was deemed necessary. The assistance provided by the recycled energy reduces the required joint torque u^{pos} to τ^{pos}. The optimization of τ^{pos} can be achieved through the solution of a convex problem as presented below:

$$\begin{aligned} &\min \|\tau^{pos}\| \\ &\text{s.t. } \omega^T u^{pos} - \omega^T \tau^{pos} = W_{rec} \end{aligned} \tag{2.16}$$

Finally, we define the CoT as the sum of the norms of the joint torques per-gait length per-time as equation 2.17. The numerator is the norms of the joint torque removed the parts that generated by the exoskeleton, L is the gait length and T is the gait period.

$$CoT = \frac{\|\tau^{pos}\| + \|u^{neg}\| - \|\tau^{neg}\|}{LT} \tag{2.17}$$

Table 2.3: Simulating Conditions. L_{gait}: the normal gait length from [57]. L_{calf}: length of calf. L_{thigh}: length of thigh. Max Height: the highest initial hip height for each gait length.

Carrying Load	20 Kg 40 Kg 60 Kg
Gait Length	$0.8L_{gait}$ $0.9L_{gait}$ L_{gait} $1.1L_{gait}$ $1.2L_{gait}$
Initial Hip Height	$0.95(L_{calf} + L_{thigh})$ $0.96(L_{calf} + L_{thigh})$ Max Height*

As the cost function in this study is not a simple quadratic equation, the boundary conditions, such as the gait length (L) and gait period (T), must be explicitly specified. To determine the minimum CoT, a parameter scan was employed in this investigation. The parameters used in this simulation are presented in table 2.3. The study employed three different models: a human model, a human model wearing a forward-knee exoskeleton, and a human model wearing a backward-knee exoskeleton. Each model was subjected to three different loads and walked with gait lengths ranging from 80% to 120% of the normal gait length. The initial height of the hip was varied between 95% of the leg length and the maximum feasible value for the given gait length. Lastly, the results with the lowest CoT were selected and will be discussed in a subsequent section.

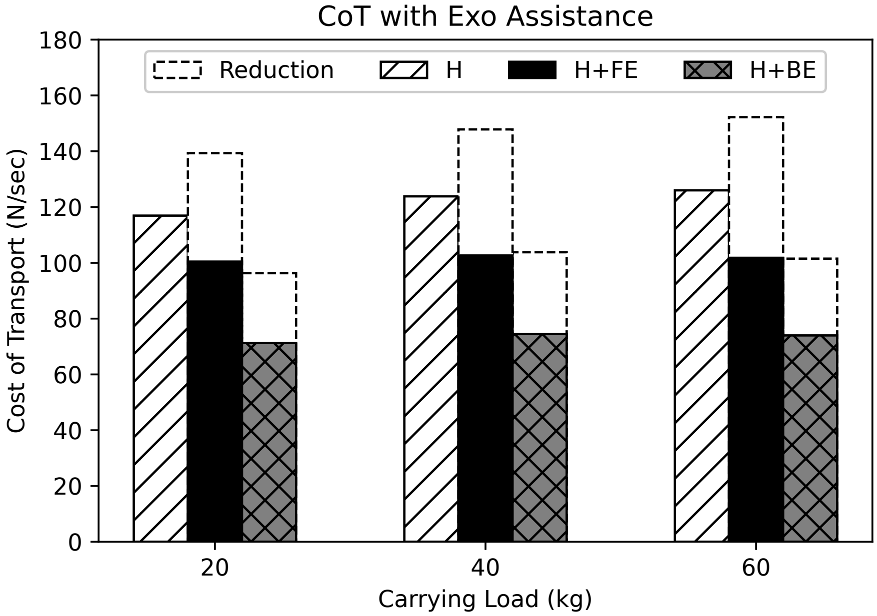

Figure 2.5: CoT of $\mu_{neg} = 0.3$, $\mu_{pos} = 0.05$ and $\mu_{neg} = 0$, $\mu_{pos} = 0$ (dashed-line). The symbols H represents the CoT of human, H+FE stands for human wearing the forward-knee exoskeleton, and H+BE stands for human wearing the backward-knee exoskeleton. The dashed-line boxes are the CoT reduction with energy recycling from the exoskeleton.

2.8 Result and Discussion

The first result of the optimization is the comparison of the models of humans wearing forward-knee exoskeleton, humans wearing the backward-knee exoskeleton, and the only-human model. Figure 2.5 shows their respective effects on CoT. The CoT reduction resulting from $\mu_{neg} = 0.3$ and $\mu_{pos} = 0.05$ is illustrated by the white dashed boxes. It is observed that the forward-knee configuration results in a significant increase in CoT due to the added weight of the exoskeleton. In fact, the CoT increment resulting from the 5 kg exoskeleton is greater than that caused by a 20 kg load placed on the back. In contrast, the backward-knee exoskeleton does not exhibit a similar effect. To explicate this dissimilarity, a thorough analysis of the torque profile for both configurations (Figure 2.6) is warranted.

Figure 2.6 displays the torque profile, where square and asterisk symbols indicate the

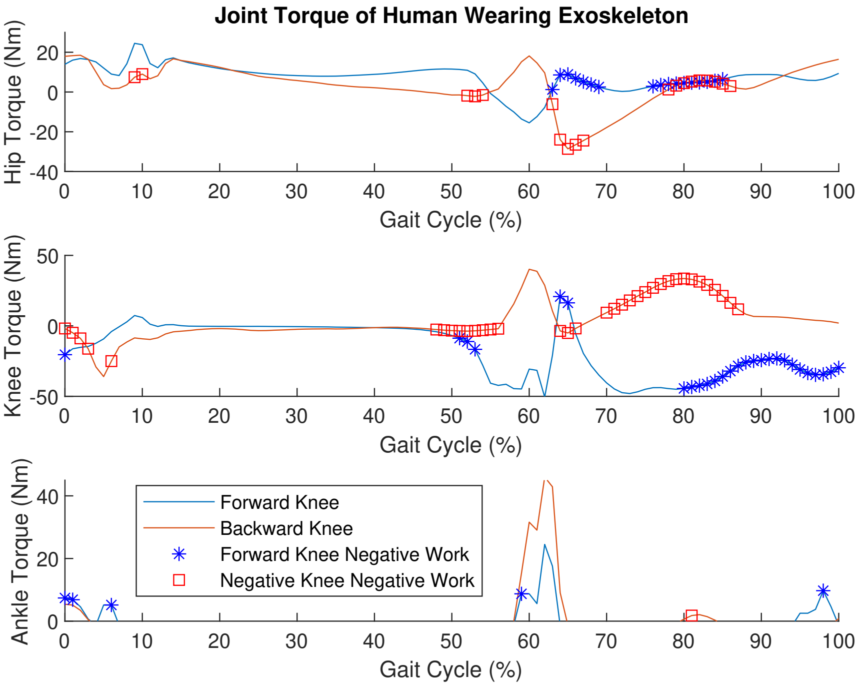

Figure 2.6: Total joint torque and negative work of human-exoskeleton system. The asterisk/square symbols suggest the joint is generating negative work.

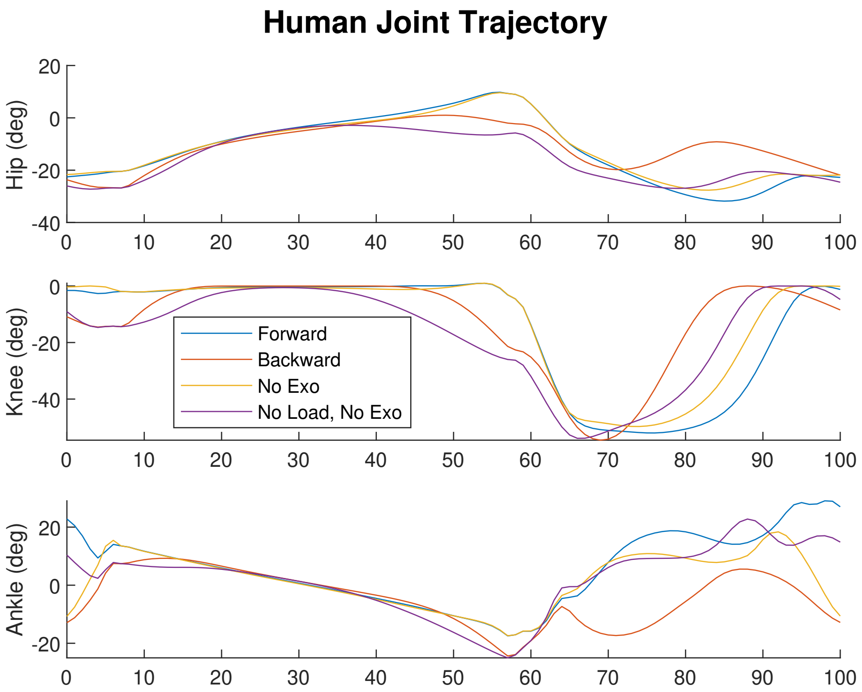

Figure 2.7: Human joint position with forward-knee exoskeleton + 40 kg load, backward-knee exoskeleton + 40 kg load, and without exoskeleton and load carrying.

torque that contributes negative work. For the forward-knee configuration, most of the negative work occurs at the knee joint, with the first occurrence happening around 65% of the gait cycle. At this point, the ankle joint provides the push-off torque, shifting the center of pressure (COP) from the rear foot to the front foot. To fully transduce the force, the rear knee must extend to counteract it. However, the knee also has to bend to create the necessary ground clearance for swinging, resulting in negative work generation during the ankle push-off. The second occurrence happens between 80% to 100% of the gait cycle, where the swinging leg decelerates before heel strike to prevent sliding. Similar, albeit smaller scale, torque can also be found in the hip joint, but torque is hardly noticeable in the ankle joint. The research team believes that this is because the elastic components, such as the Achilles tendon, generate the required negative work.

On the other hand, the negative work required to wear the backward-knee exoskeleton is considerably lower, as evident from Fig. 2.6. The researchers suggest that this is due to the backward-knee exoskeleton acting as a ”counterweight” during the swing phase, thereby reducing the torque required to generate negative work. Moreover, for the backward-knee exoskeleton, the deceleration of the swing leg initiates at an earlier stage (70% of the gait cycle) compared to the forward-knee exoskeleton. This early deceleration can be attributed to the joint trajectory of the user, as depicted in Fig. 2.7. The figure indicates that, while carrying loads with the forward-knee exoskeleton, the knee remains in a singular position for a longer duration than it does without loads (difference in knee joint angle from 50% to 60% of gait cycle). This is due to the fact that the forward-knee configuration necessitates a larger moment arm at the rear ankle to shift the COP/COM to the leading foot. However, a prolonged singular position necessitates greater acceleration/deceleration during the swing phase. Conversely, the backward-knee configuration achieves the same goal without requiring a prolonged singular position. By bending the leading leg's knee, the COP/COM naturally shifts to the front leg. This behavior is not feasible with the forward-knee configuration, as the COM moves backward when the knee bends. Consequently, when wearing the backward-knee exoskeleton, the user only needs to ”sit” on the front leg, instead of using the rear ankle to ”push” and propel the COM. This property also reduces the impact loss during heel strike. The trajectory of the COM (Fig. 2.8) indicates that, during heel strike, the vertical position of the COM is lower when wearing the backward-knee exoskeleton, and is proportional to the load it carries. This is because the leading knee genuflects to absorb the impact, as can also be observed in the torque profile of the knee joint around 0% to 5% gait cycle (Fig. 2.6). By absorbing the impact through knee bending, the energy loss during heel strike can be recovered. In addition to these benefits, the backward-knee exoskeleton also increases the mechanical work during ankle push-offs. Fig. 2.9 presents the joint mechanical power of the user when wearing the forward-knee or the backward-knee exoskeleton. Although the ankle torques are of similar magnitude, the backward-knee exoskeleton generates five times more mechanical power. This difference can be attributed to the angle between the GRF and the

Table 2.4: Angle between GRF and the ground under different loads. BW refers to *body weight*.

Knee \Load (BW)	30.77%	61.54%	92.31%
Forward(°)	61.9	65.9	51.35
Backward(°)	51.34	51.34	51.34

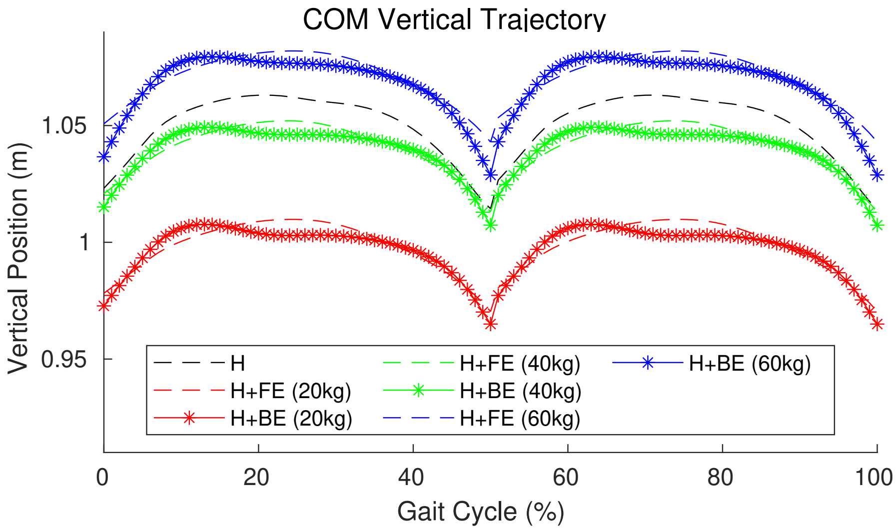

Figure 2.8: Center of mass trajectory.

ground (Table 2.4), which is smaller when wearing the backward-knee exoskeleton, resulting in a larger moment arm for the system.

2.9 Conclusion

In this chapter, we present a trajectory-optimization approach for load-carrying walking aided by exoskeletons. We integrate collision-based GRF in discrete Lagrangian dynamics to determine minimal-effort-walking trajectories. The results indicate that the backward-knee exoskeleton reduces the normal-walking CoT by 35% under the assumed efficiencies of $\mu_{resist} = 0.3$ and $\mu_{recycle} = 0.05$. This result is superior to the forward-knee exoskeleton, which only reduces the CoT by 15%. The observed difference is attributed to the better utilization of the knee joint during heel strike and the longer moment arm for the GRF

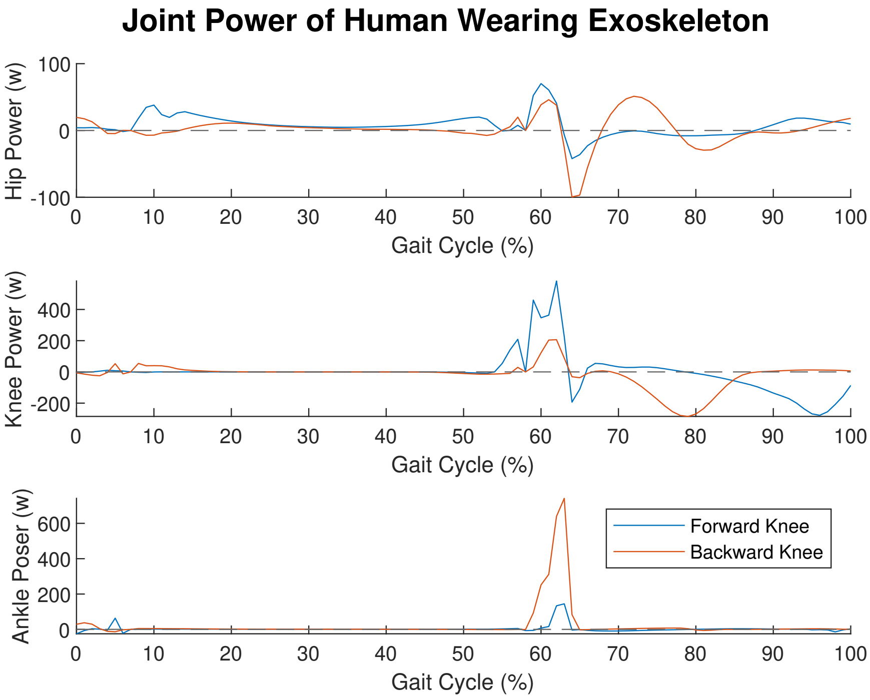

Figure 2.9: Joint power under different loads.

during ankle push-off in the backward-knee configuration. Therefore, when designing an exoskeleton to aid load-carrying walking, the backward-knee configuration is preferred.

CHAPTER 3

Pneumatic Actuators for Exoskeleton

3.1 Introduction

Human walking is considered to be energy-inefficient owing to energy loss during heel strikes and the negative work performed by the joints. Researchers have demonstrated that the addition of compliance to bipedal robots can reduce energy consumption during walking [59]. In recent years, lightweight, spring-like structures have been developed that aim to scavenge energy from these processes by controlling their compliance to absorb the collision or generate negative work [16]–[18], [25]–[27]. Nonetheless, these devices are restricted to recycling energy in the same joint from which it is scavenged, which is not optimal for joints with asymmetric torque profiles, such as the knee and ankle. To overcome this limitation, Miskovic [60] proposed the use of pneumatic cylinders instead of springs to absorb negative work during the gait cycle, allowing the energy to be stored as pressurized air and applied to different joints. However, this device lacks control over the impedance it generates, which could result in incomplete absorption of energy or excess energy input by the user.

Impedance and admittance control have been investigated in the development of wearable robots [61]. Rather than controlling either the position or the force, regulation is focused on the relationship between position and force. The use of pneumatic actuators for impedance/admittance control has two advantages over traditional motor-based actuators: natural compliance and lower energy consumption. Prior studies have explored pneumatic impedance/admittance control, including the use of air chamber volume to control impedance

[62] and the use of air cylinders and air dynamics to control actuator stiffness for haptic devices [63].

Pneumatic actuators have been extensively employed in various applications due to their high force output at low speeds and high force-to-weight ratio. This makes them a preferred choice for robots and wearable robotic devices [2], [64]–[67]. Furthermore, bio-inspired actuators, such as artificial muscles, are frequently powered by pneumatic systems [59], [68]–[70]. The control of pneumatic systems is typically achieved through pneumatic valves, which are broadly categorized as proportional valves and solenoid valves [71]. Proportional valves are generally used in pneumatic servo systems owing to their linear control capabilities, enabling continuous flow control via the adjustment of the air passage width [72], [73]. Nonetheless, proportional valves are more expensive, with prices often exceeding \$1000 USD per valve, and have longer response times ($>$ 5 ms). In contrast, solenoid valves are considerably cheaper, costing around one-tenth of proportional valves, and have faster response times of approximately 2 ms [74]. However, their binary nature limits their precision, rendering them less suitable for high precision control applications, such as active suspension systems [75].

To address the limitations of solenoid valves, Ye introduced low-pass filtering to pneumatic control [76]. While solenoid valves allow for fluid to pass in a discrete manner, the compressibility of air allows for high-frequency operations to be filtered down to steady flow. By utilizing pulse width modulation (PWM) commands to turn the solenoid valves on and off, the flow rate can be continuously controlled by adjusting the duty cycle. However, the relationship between the duty cycle and flow rate is highly nonlinear and involves states that are difficult to measure. Unlike electrical motors, where the output torque is a function of input voltage and current, the flow rate in pneumatic systems depends on operating conditions such as pressure and temperature in each chamber. Traditional pneumatic servo control models often rely on simplifications, such as assuming that the air is an ideal gas, pressure and temperature are uniform in each chamber, and connections and leakages do not affect the dynamics of the air [71]. Some studies also assume that the process is adiabatic, as heat transfer is negligible over short periods of time [77], [78]. Miskovic [60] even suggests that this process can be viewed as isothermal. These simplifications allow for the creation of nonlinear dynamical models with measurable states while avoiding the need to measure inaccessible heat transfers.

Pneumatic systems have traditionally been controlled using linear proportional-integral-derivative (PID) control with nonlinear mapping [79]. However, this method is only suitable for isolated systems with fixed physical properties, where there are no external forces or constant loads. To address this limitation, sliding mode control (SMC) has been proposed as an alternative approach to improve control robustness [80], [81]. SMC has been applied to both solenoid and proportional valves, with solenoid valves being more popular because they are easier to set up to open on one side of the switching surface and close on the other. To prevent frequent switching on and off as states approach target values, Nguyen [82] introduced a dead-band near the sliding surface. However, determining the correct switching surface can be challenging since the dynamical model of the system may be difficult to obtain. For example, Andrikopoulos used multiple dynamical models for a single system in different phases to achieve model predictive control on pneumatic artificial muscles [83]. Generating a precise dynamical model can be difficult due to various factors such as the actuators' rise time, volume of reservoirs, length of tubing, and diameter of the valve's orifice that can differ from one part to another [84]. These parameters can be difficult to quantify, and the orifice of the valve is often undetermined during valve operation. Additionally, assuming that air behaves like an ideal gas or that temperature is uniform, particularly at high speeds, is unrealistic, and this can affect the model's accuracy. As a result, most pneumatic servo control operates at a slower speed compared to servo motor control to avoid the latency and transient effects that can occur in pneumatic systems.

Various data-driven model generation methods have been developed to improve the accuracy of pneumatic system models. Zhang [85] used piece-wise-linear functions in different phases to approximate system dynamics, with coefficients obtained through data analysis of simulation data. Vailati [86] improved modeling accuracy by calculating the model with real measurements, using polynomial functions to substitute the nonlinear flow rate equation, and finding all coefficients with in-valve pressure sensors. To achieve greater accuracy, the mechanical properties of pneumatic valves were also taken into account by Messina [78], who used a laser sensor to precisely measure solenoid valve displacement. However, these calibration methods often require additional measurements and are not ideal for online calibration of closed systems. In addition, polynomial functions, which can describe the dynamics, often have a lack of physical interpretation and require a large number of training data. Recently, the sparse identification of nonlinear dynamics (SINDy) framework has gained attention in nonlinear control studies [87]. In the SINDy framework, a library of all possible candidates is generated to reconstruct the system's dynamics, and sparse regression techniques such as Lasso are used to select the fewest terms. By including more prior knowledge, the size of the training data is significantly reduced, and the resulting model can be interpreted physically. This approach has shown success in finding the Jacobian of complex robotic systems [88], with the physical interpretation aiding derivative-based control methods and model predictive control [89]–[91].

In this chapter, we present a low-cost pneumatic actuator for wearable devices. Our actuator offers several improvements over previous designs:

- We demonstrated that the physical parameters of the system can be accurately estimated using a small training dataset. This eliminates the need for measuring inaccessible or non-quantifiable parameters. To achieve this, we employed a model that incorporates knowledge of the fundamental physics underlying the system's dynamics. This approach allows for improved interpretation of the results and avoids overfitting.
- The controller accounts for the natural delays between valve actuation and flow rate with model predictive control.
- The energy used for generating negative work can be recycled and reused to assist with

positive work.

By meeting these objectives, we believe that our actuator is optimized for use in lower-limb exoskeletons.

3.2 Energy Recycling from Pneumatic Systems

3.2.1 Mechanical Design

The wearable device designed to recycle energy from human walking must meet two objectives: absorption of impacts and generation of negative work. Pneumatic systems can be used to achieve these objectives, utilizing precise pressure control to create an air-spring during the swing phase and using this air-spring for active impedance control during impact (heel strike) absorption and negative work. The scavenged energy will be used to assist the ankle joint in the opposing leg. The whole operating concept is shown in Fig. 3.1.

In order to effectively recycle energy from human walking, a wearable device must accomplish two tasks: absorb the impacts of walking and generate negative work. One method to achieve these objectives is through the use of pneumatic systems, which rely on precise pressure control to create an air-spring during the swing phase of walking. This air-spring can then be utilized for active impedance control during impact absorption, particularly during heel strike. By scavenging this energy, the device can assist the ankle joint in the opposing leg. The operational concept of the device is depicted in Figure 3.1.

Although our study aims to minimize energy consumption using pneumatic actuators, it is worth noting that pneumatic actuation can be energy-inefficient. The force output of a pneumatic cylinder is determined by the pressure difference and area between the two chambers of the cylinder, which are pressurized and depressurized during a typical pneumatic circuit [71]. However, releasing pressurized air can result in energy loss. To address this issue, our design incorporates a pneumatic loop between the two chambers of the cylinder (Figure

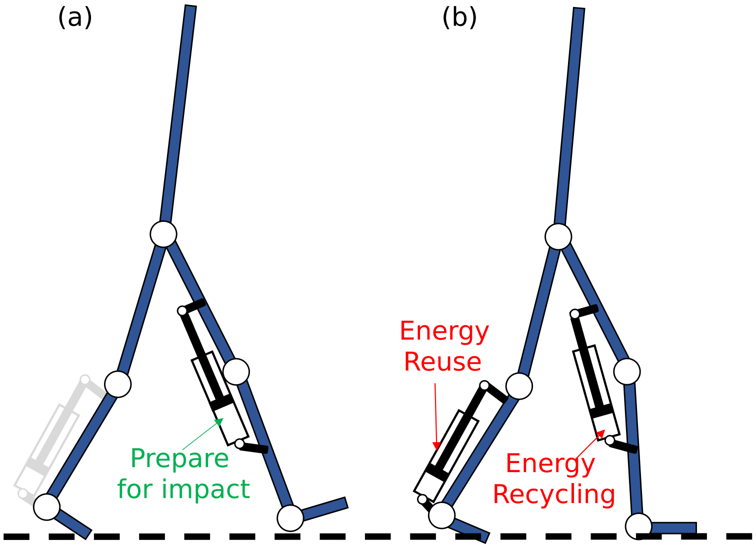

Figure 3.1: Control objectives for energy recycling with wearable pneumatic systems. The device needs to be able to (a) create an air spring at the knee joint with pressure control and (b) recycle the negative work with impedance control at the knee joint, and reuse the energy in the oppose ankle joint.

3.2). This allows for the reduction of output force by balancing the pressure across the piston or directing pressurized air to a lower pressure reservoir for later use, rather than releasing it. Simulation results indicate that the knee and ankle joints primarily output torque in a single direction, with the exception of the hip joint [92]. Therefore, our actuator is designed to regulate force output in only one direction, as demonstrated by the valve operating logic shown in Figure 3.3. Operations that increase force output are illustrated in Figures 3.3a and 3.3b, while operations that decrease force output are shown in Figures 3.3c and 3.3d. The controller will select the optimal operation that minimizes energy consumption, specifically by reducing pressurized air exhaustion.

3.2.2 Bio-inspired Pneumatic Actuator

Despite air is compressible, the use of solenoid valves to control a pneumatic cylinder still produces discrete force outputs. To mitigate this issue and conserve energy, we have added a mechanical spring to the end of the cylinder, similar to how human tendons act as

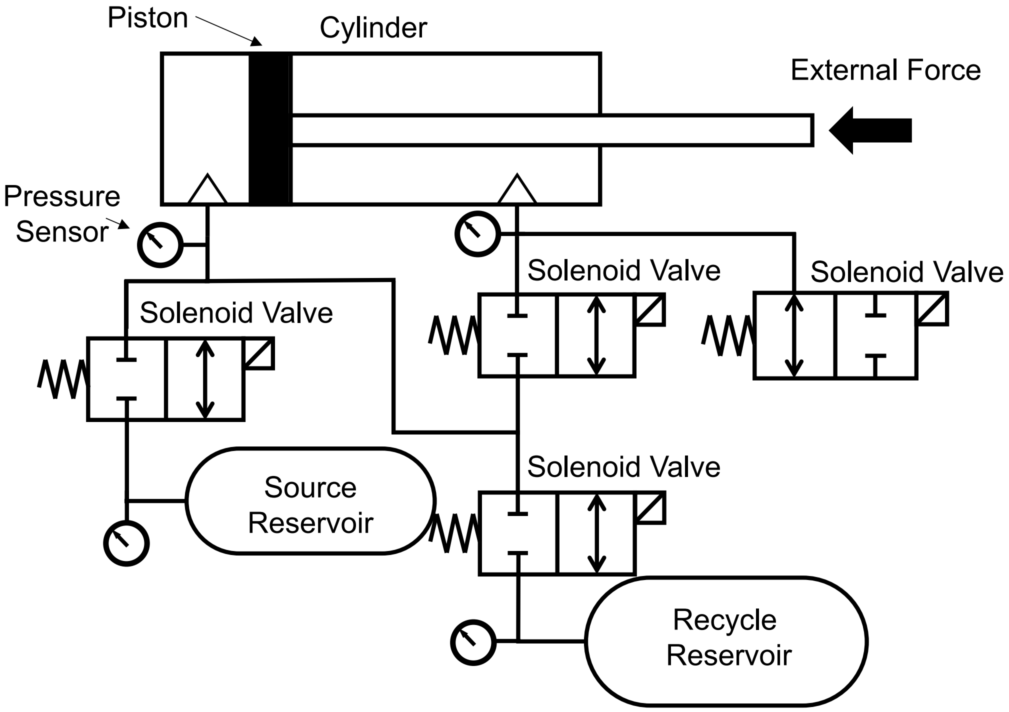

Figure 3.2: Pneumatic actuation/recycle circuit for single joint.

”buffers” to muscles [93] (Figure 3.4). To simplify the actuator, we do not directly measure the compression of the spring, but rather the entire length of the actuator. The length of the chamber (x) can be estimated using Equation (3.1). It is worth noting that, in the context of lower-limb wearable systems, the mass of the piston rod is considered negligible in relation to the actuation forces required.

$$x = L_{tot} - \frac{P_{ext}A_{ext} - P_{ret}A_{ret}}{k} \tag{3.1}$$

The definition of the symbols used in (3.1) is shown in Fig. 3.4. P_{ext} is the pressure that extends the cylinder, P_{ret} is the pressure that retracts the cylinder, k is the spring constant, μ_k is the dynamic friction coefficient, x is the position of the piston, and A_{ext}, A_{ret} are the cross-section area of each side of the piston. The output force of the cylinder F can be defined as (3.2):

$$F = P_{ext}A_{ext} - P_{ret}A_{ret} - \mu_k\dot{x} \tag{3.2}$$

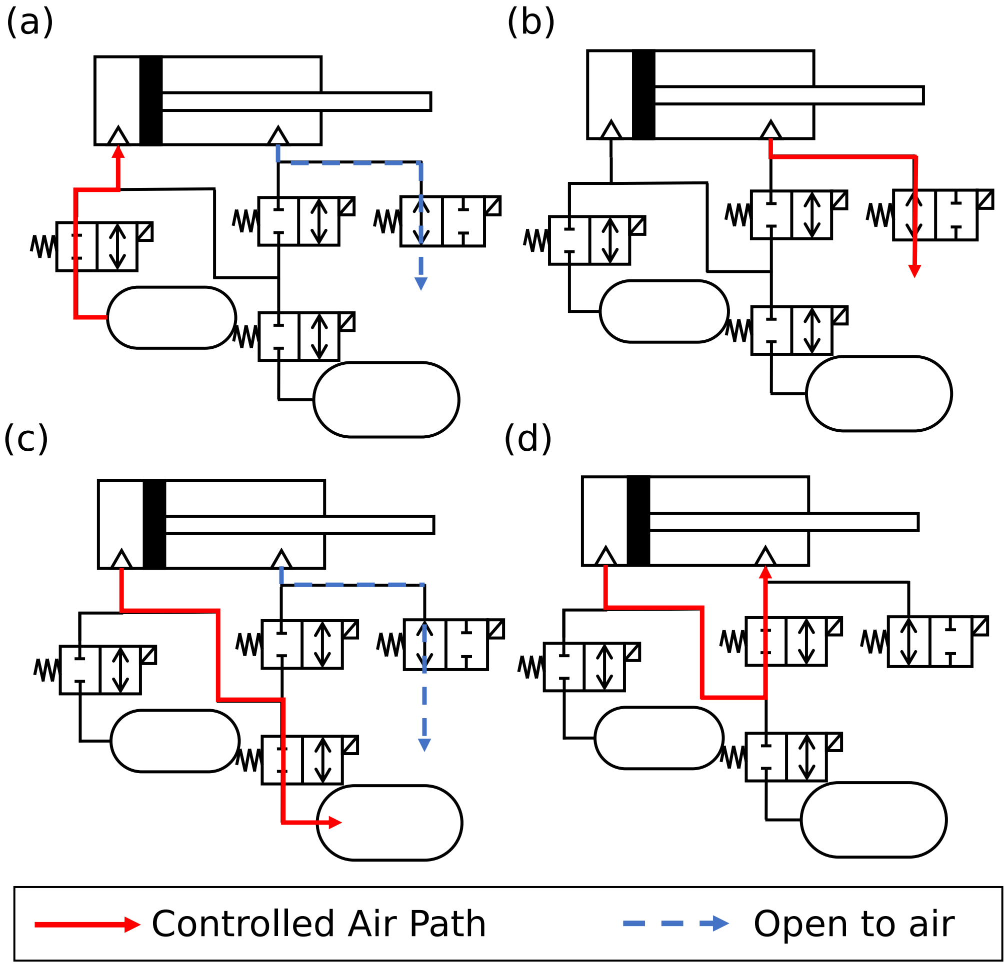

Figure 3.3: Solenoid valve operating logic for (a) Increasing force output by draining pressurized air from the reservoir. (b) Increasing force output by decreasing pressure in the cylinder. (c) Decreasing force output by discharging air to other chambers in the system. (d) Decreasing force output by balancing the pressure across the piston.

3.2.3 Pneumatic Control with Delayed Differential Equations

The dynamics of pneumatic systems can be described using the principles of thermal dynamics and the conservation of energy. The relationship between pressure, volume, external forces, temperature, the mass of the air, and the flow rate can be expressed in the following equation:

$$P\triangle V + \triangle P V + F\triangle x + c_p\triangle m T + c_v m\triangle T = 0 \tag{3.3}$$

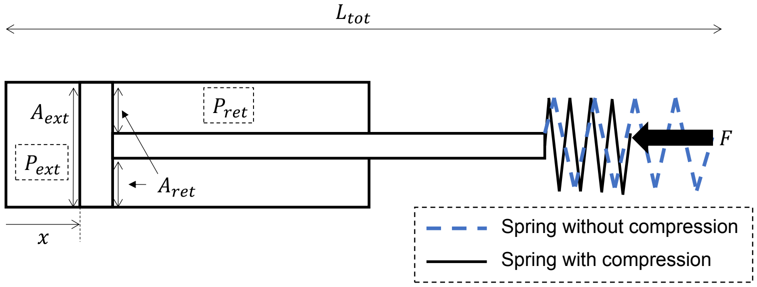

Figure 3.4: Definitions of dimensions of the pneumatic actuator in (3.1).

P is the pressure, V is the volume, F is the external force, t is time, c_p is the specific heat constant of constant pressure, T is the temperature of the gas in Kelvin, m is the mass of the air in the cylinder, and symbols with the $\triangle$ prefix represents the changes of the following quantity. The mass's rate change, or the "flow rate", can be described as the function of the upper stream pressure, lower stream pressure, and the temperature of the upper stream [71] as (3.4).

$$Q = \frac{\triangle m}{\triangle t} = CP_u\sqrt{\frac{T_u}{T_d}}W(p_u, p_d) \tag{3.4}$$

P_u, T_u, P_d, T_d are the upstream and downstream pressure/temperature. C is the product of sonic conductance and the density of air. The function W describes the "choking" effect caused by the shockwave when the flow rate is supersonic, which is defined as (3.5).

$$W(p_u, p_d) = \begin{cases} 1 & if \frac{P_d}{P_u} > \beta \\ \sqrt{1 - (\frac{\frac{P_d}{P_u} - \beta}{1-\beta})^2} & if \frac{P_d}{P_u} \leq \beta \end{cases} \tag{3.5}$$

β is the critical pressure ratio corresponding to the orifice, which are both constants that depend on the mechanical properties.

A significant limitation of the approach described above is the assumption that the temperature within the chamber is uniform and measurable. However, in reality, integrating temperature sensors into each chamber can be challenging, and local temperature measurements are often the only viable option. This presents a fundamental challenge to the validity of the model presented in Equation (3.3).

Another challenge pertains to accurately estimating the sonic conductance and critical pressure ratio. While these quantities are generally treated as constants, they can vary based on specific circumstances, such as the type of valves used and the composition of the atmosphere. Furthermore, the relationship between the flow rate and the solenoid valve's switching is not well understood. While some studies have suggested that the flow rate is zero when the valve is off [85], [94], this overlooks the fluid's momentum. In reality, there are significant delays between the flow rate and the valve's activation. Figure 3.5 illustrates the relationship between the pressure difference and the pressure gradient after the valve is opened, where the upstream-downstream pressure difference is proportional to the flow rate [94], [95]. The maximum pressure change does not occur at the maximum pressure difference when the upstream and downstream chambers are connected, indicating that the fluid requires time to "accelerate." To account for this latency in the dynamical model, we define the flow rate Q at time n (Q_n) as a discrete delayed differential equation that incorporates the history of pressures and the valve's duty cycle, as shown in Equation (3.6).

$$
\begin{aligned}
Q_n =& Q(\phi_{n-t_d}, \phi_{n-t_d+1}, \phi_{n-t_d+2}, ...\phi_n) \\
\phi_i =& \phi_i(P_{u,i}, P_{d,i}, u_i)
\end{aligned}
\tag{3.6}
$$

While t_d is the maximum delay in the system (i.e., the earliest states that affect the current dynamics), and ϕ_i is a nonlinear equation that describes how the states at i affect the current dynamics. Unfortunately, such a relationship is affected by physical characteristics and cannot be easily defined. In this study, we will use a data-driven method i.e. sparse identification of nonlinear dynamics (SINDy) to retrieve the dynamical equations.

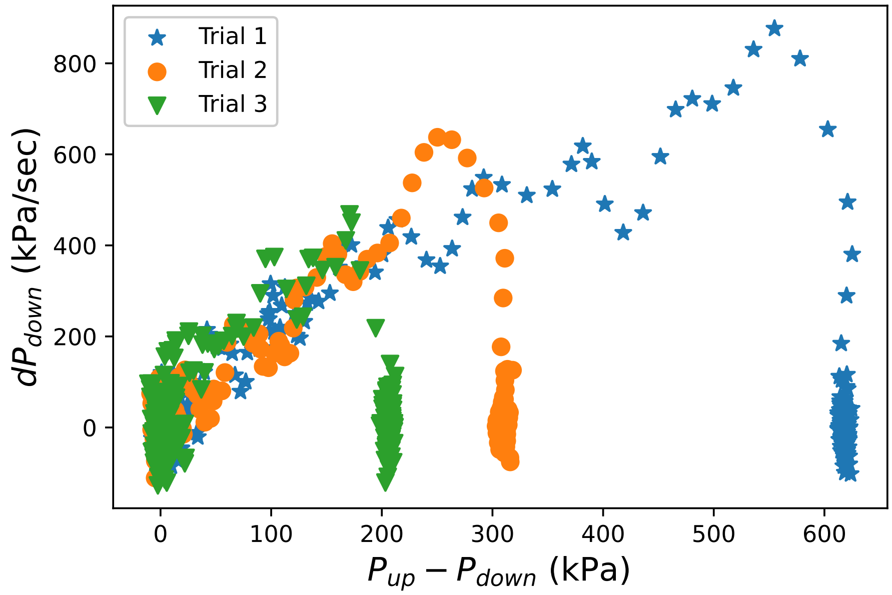

Figure 3.5: Downstream pressure's rate of change v.s. pressure difference between upstream and downstream chambers when opening the valve. The beginning of each trial started from the lower right, as we can see there are delays at the beginning at every trial since the max flowrate does not occur when the pressure difference is the max.

3.2.4 SINDy of Pneumatic Systems

Sparse identification of nonlinear dynamics (SINDy), is a data-driven method which finds the dynamical equations of a system with the prior knowledge of the system's physics. The core principle of SINDy involves generating candidate models based on prior knowledge and selecting the model with the fewest terms that can accurately describe the collected data. To simplify the model for our purposes, we made the assumption that all temperature-related terms are constant. This assumption allows us to assume that the ratio of upstream to downstream temperatures is constant and that $\triangle T = 0$ in Equation (3.3). This is a reasonable assumption, as the process occurs in less than a second, and temperature variations are therefore limited. Moreover, the ratio of temperatures is nearly constant at room temperature, given the use of Kelvin as the unit. By merging all constants in the dynamical equation, we defined the rate of change of pressure as shown in Equation (3.7).

$$\triangle P_n = \frac{Q'_n \triangle t}{V_n} \tag{3.7}$$

Q'_n is a function that has the identical structure as (3.6) but includes all constants. To keep the expression consistent, we denote each ϕ terms in Q'_n as ϕ'.

The second step is to include the control input into the model, and decouple the constant and varying terms. From the mechanical perspective, changing the duty cycle of the solenoid valve's PWM command is similar to changing the orifice's area. Inspired by (3.3), (3.4), (3.5) and (3.6), we can rewrite each ϕ' in (3.7) as (3.8):

$$\begin{aligned}
&\phi'_n(P_{p,n}, P_{d,n}, u_n) \\
= \quad & \eta_0 \underbrace{P_{u,n} - P_{d,n})u_n}_{d_{0,n}} \\
& + \eta_1 \underbrace{(P_{u,n} - P_{d,n})\sqrt{1 - (\frac{P_{d,n}}{P_{u,n}})^2}u_n}_{d_{1,n}} \\
& + \eta_2 \underbrace{((P_{u,n} - P_{d,n})\sqrt{1 - (\frac{P_{d,n}}{P_{u,n}})^2}u_n)^2}_{d_{2,n}} \\
& + \eta_3 \underbrace{(P_{u,n} - P_{d,n})\sqrt{(1-b)^2 - (\frac{P_{d,n}}{P_{u,n}} - b)^2}u_n}_{d_{3,n}} \\
& + \eta_4 \underbrace{(P_{u,n} - P_{d,n})\sqrt{(1-b)^2 - (\frac{P_{d,n}}{P_{u,n}} - b)^2}u_n^2}_{d_{4,n}}
\end{aligned} \tag{3.8}$$

u is the duty cycle of the valve, $d_{i,n}$ and η_i, $i = 0, 1, 2, 3, 4$ are the potential candidate of the varying terms in the dynamical equation and its coefficients. b is a parameter that is similar to the critical pressure ratio and is chosen during the model validation process. In our experiments, we found that $b = 0.001$ produced accurate models, regardless of the specific hardware being used. As shown in (3.7), all η are independent of the chamber's volume V, which allows us to calibrate the η with a fixed volume via SINDy, which can be realized with sparse regression as shown in (3.9) and (3.10):

$$\underbrace{\begin{bmatrix} \triangle P_{u,n} & \triangle P_{d,n} \\ \triangle P_{u,n+1} & \triangle P_{d,n+1} \\ \vdots & \vdots \end{bmatrix}}_{y} = \underbrace{\begin{bmatrix} D_0 & D_1 & \dots & D_n \\ D_1 & D_2 & \dots & D_{n+1} \\ \vdots & \vdots & & \vdots \end{bmatrix}}_{A} \eta \tag{3.9}$$

$$D_n = \begin{bmatrix} d_{0,n} & d_{1,n} & d_{2,n} & d_{3,n} & d_{4,n} \end{bmatrix}$$

$$\eta = \begin{bmatrix} \eta_0 & \eta_1 & \eta_2 & \eta_3 & \eta_4 \end{bmatrix}^T$$

$$\min_{\eta} ||y - A\eta||_2^2 + \alpha||\eta||_1 \tag{3.10}$$

α is a hyper-parameter that is chosen with the validation test. D_n is the vector of all candidates generated from the measurements. Note that all measurements are normalized to reduce the effects of differences in scales. By solving η, we can rewrite the dynamics as a discrete differential equation:

$$x_{n+1} = \frac{\triangle t}{V_n} \begin{bmatrix} D_{n-d} & D_{n-d+1} & \dots & D_n \end{bmatrix} \eta + x_n \tag{3.11}$$

Having obtained a symbolic expression of the system dynamics, we can use it to predict the future and calculate the optimal control input with the model predictive controller that will be detailed explained in the next section.

3.2.5 Model Predictive Control of Pneumatic Systems

Pneumatic systems often exhibit significant latency, which can lead to overshooting when using traditional feedback control. To address this issue, we introduced the use of model predictive control (MPC) to control the pressure by utilizing the history of the measurements and the control inputs. MPC allows us to anticipate future behavior of the system and adjust the control inputs accordingly, resulting in more precise pressure control. From (3.11), we can define the prediction as (3.12).

$$\begin{aligned} y_n &= H x_n \\ x_{n+1} &= f(x_n, u_n, x_{n-1}, u_{n-1}, \dots, x_{n-d}, u_{n-d}) \\ x_n &= \begin{bmatrix} P_{u,n} & P_{d,n} \end{bmatrix} \end{aligned} \tag{3.12}$$

y is the state that needs to be controlled. H is the observation matrix since in the real-world application, we only need to control either the upstream or the downstream pressure.

In order to solve the optimal control sequence $u_n, u_{n+1}, \dots$, we linearly approximate the future state and formulate the MPC problem into a quadratic optimization problem. The prediction of the states can be approximated with linearized equation (3.11).

$$
\begin{aligned}
\hat{x}_{n+1} &= f(p_n) + \frac{\partial f}{\partial u_n}|_{p_n}(u_n - \bar{u}) \\
\hat{x}_{n+2} &= f(p_{n+1}) + \frac{\partial f}{\partial x_n}|_{p_{n+1}}(x_{n+1} - \bar{x}_{n+1}) \\
&\quad + \frac{\partial f}{\partial u_n}|_{p_{n+1}}(u_{n+1} - \bar{u}_{n+1}) + \frac{\partial f}{\partial u_{n-1}}|_{p_{n+1}}(u_n - \bar{u}) \\
&\vdots \\
\hat{x}_{n+k} &= f(p_{n+k-1}) + \frac{\partial f}{\partial x_n}|_{p_{n+k-1}}(x_{n+k-1} - \bar{x}_{n+k-1}) \\
&\quad + \frac{\partial f}{\partial u_n}|_{p_{n+k-1}}(u_{n+k-1} - \bar{u}) \\
&\quad + \cdots + \frac{\partial f}{\partial u_{n-k+1}}|_{p_{n+k-1}}(u_n - \bar{u})
\end{aligned}
\tag{3.13}
$$

$\hat{x}_n$ is the prediction of the state variable x. p_i are the points where we linearize the equation.

$$
\begin{aligned}
p_n &= (x_n, \bar{u}, x_{n-1}, u_{n-1}, \ldots, x_{n-k}, u_{n-k}) \\
p_{n+1} &= (\bar{x}_{n+1}, \bar{u}, x_n, \bar{u}, \ldots, x_{n-k+1}, u_{n-k+1}) \\
p_{n+2} &= (\bar{x}_{n+2}, \bar{u}, \bar{x}_{n+1}, \bar{u}, \ldots, x_{n-k+2}, u_{n-k+2}) \\
&\vdots \\
p_{n+k-1} &= (\bar{x}_{n+k-1}, \bar{u}, \bar{x}_{n+k-2}, \bar{u}, \ldots, \bar{x}_n, \bar{u})
\end{aligned}
\tag{3.14}
$$

$\bar{x}_n, \bar{u}$ is the nominal assumption of the future state. Mathematically, the accuracy of linear approximation decreases as x_n, u_n deviate from $\bar{x}_n, \bar{u}$. In practice, we found that using linear interpolation between the current states' values and the desired states' values as $\bar{x}_n$ resulted in more accurate estimations.

With the above linearization, one can rewrite the estimation of the future states as (3.15):

$$
\begin{aligned}
\hat{x}_{n+1} =& A_n + B_n u \\
\hat{x}_{n+2} =& A_{n+1} + B_{n+1} u \\
& \vdots
\end{aligned}
\tag{3.15}
$$

while $u = \begin{bmatrix} u_n & u_{n+1} & \dots & u_{n+k-1} \end{bmatrix}^T$ The optimal control inputs can be calculated by the following quadratic optimization:

$$
\begin{aligned}
& \min_{u} \sum_{i=n+1}^{N} ||\hat{y}_i - y_i^{des}||_2^2 \\
& s.t. \\
& \quad \hat{y}_i = H\hat{x}_i \\
& \quad \hat{x}_{i+1} = A_i + B_i u \\
& \quad 0 \leq u_i \leq 1
\end{aligned}
\tag{3.16}
$$

$\hat{y}$ is the estimation of y while y^{des} is the desired value. u_i is bounded between 0 and 1 since the control inputs are normalized.

3.3 Experiment

The experiments conducted in this study were organized into three parts. In the first part, a model was trained by activating solenoid valves with fixed-duty cycles. The data collected was then used to train a discrete delayed differential model for use in Model Predictive Control (MPC). In the second part, the MPC controller was implemented to regulate pressure in preparation for impact. Finally, in the third part, the performance of the MPC in energy recycling with impedance control during impact was verified. The experimental setup utilized for these experiments is depicted in Figure 3.6, and a list of the parts used is provided in

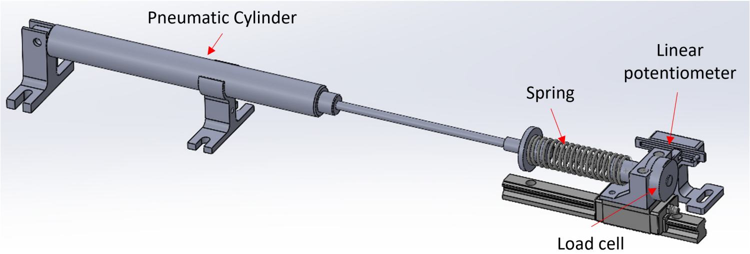

Figure 3.6: Experiment setup.

Table 3.1.

Table 3.1: Parts used in Experiment

Source Reservoir	Festo CRVZS-0,1
Recycle Reservoir	Festo CRVZS-0,1
Pneumatic Cylinder	Clippard UDR-14-6
Solenoid Valve	Festo MHE3-MS1H-3/2G-1/8K
Load Cell	FC2311-0000-0050-L
Spring Constant	$9.702 N/mm$

3.3.1 Model Training and Verification

The model is trained with SINDy as described in the previous section. The upstream and downstream pressure were recorded while operating the valve in fixed duty cycles. The pneumatic cylinder's volume was maintained constant during the training. The training results are shown in table 3.2. The R2 accuracy shows the SINDy algorithm reached 90.58% accuracy on the training set, and avoids over-fitting with a validation accuracy of 88.2%. The total number of samples are less than 2000, collected with 100Hz sampling rate within 10 minutes.

Table 3.2: Top 5 Model Accuracy

	Number of Samples	R2 Accuracy(%)
Training Accuracy	1440	90.58
Validation Accuracy	360	88.2
Test Accuracy	600	86.44

3.3.2 Pressure Control

After the model is trained, it is programmed for pressure regulation. We test four different scenarios that are listed in table 3.3. For each scenario we repeated the test for 10 times, and calculate the mean error and variance.

The above MPC is programmed with University of Oxford's Operator Splitting Quadratic Program (OSQP) [96] on a Raspberry pi 4B patched with PREEMPT_RT real-time kernel. The sampling rate is 100 Hz and the measurements are filtered with fifth-order 30 Hz low-pass filter.

Table 3.3: Test scenarios for pressure regulations.

	Initial Pressure (kPa)	Target Pressure (kPa)
Case 1	0	200
Case 2	0	300
Case 3	300	450
Case 4	300	320

3.3.3 Impedance Control with Energy Recycling

As shown in Fig. 3.6, a load cell is placed on top of a guided rail to verify the force output's accuracy. The experiment's goal is to test if the controller can modulate the virtual impedance it created with energy recycling. The desired force output is defined as:

$$F_{des} = k_{imp}x + F_{init} \tag{3.17}$$

F_{des} is the desired force output, k_{imp} is the virtual impedance, x is the piston's displacement, and F_{init} is the force output when the cylinder is fully extended ($x = 0$). The F_{init} and k_{imp} are set as Table 3.4. Since the MPC requires reference inputs for the full time horizon, we will predict the future desired force based on the current speed, the adjusted F_{des} is now:

$$F_{des,i} = k_{imp} \times (x + idx) + F_{init}, i \in (0, n) \tag{3.18}$$

dx is the piston's travel distance per unit time, and n is the time horizon of the MPC controller.

At the beginning of the test, the cylinder is pressurized to reach F_{init}, and manually compressed until it reaches the spring's equilibrium point to remove the effect of the spring and have full control of the force output. After that, an impact force is applied to compress the cylinder. During the impact, the controller regulates the pressure to generate the virtual impedance. The efficiency of the system is defined as *Energy Reused Rate* μ (3.19), which is the energy gain in both the cylinder ($\triangle E_{cylinder}$) and recycle reservoir ($\triangle E_{rec}$) over the sum of energy loss in source reservoir ($\triangle E_{source}$) and the work of external force ($\triangle E_{mech}$).

$$\text{Energy Reused Rate: } \mu = \frac{\triangle E_{cylinder} + \triangle E_{rec}}{\triangle E_{Source} + \triangle E_{mech}} \tag{3.19}$$

Table 3.4: Energy Utilization during impedance control

Initial force: 50 N		Impedance: 5000 N/m		
	Energy Consume (J)	External Impact (J)	Energy Reused (J)	Energy Reused Rate μ
Trial 1	4.745	0.183	4.206	0.886
Trial 2	5.676	0.195	5.083	0.895
Trial 3	4.322	0.201	4.026	0.932
Trial 4	5.871	0.336	5.188	0.884
Trial 5	7.246	0.348	6.033	0.833

3.4 Result

Figure 3.7 displays the results of pressure control. The upper plot illustrates the error between the control pressure and the command pressure as a function of time. The lower plot shows the estimated pressure calculated by the MPC controller. The results demonstrate that the MPC controller was able to regulate the pressure within ±10 kPa, which is less than 5% of the desired value. Furthermore, the process was energy-efficient, as there was no wastage of energy due to exhaustion.

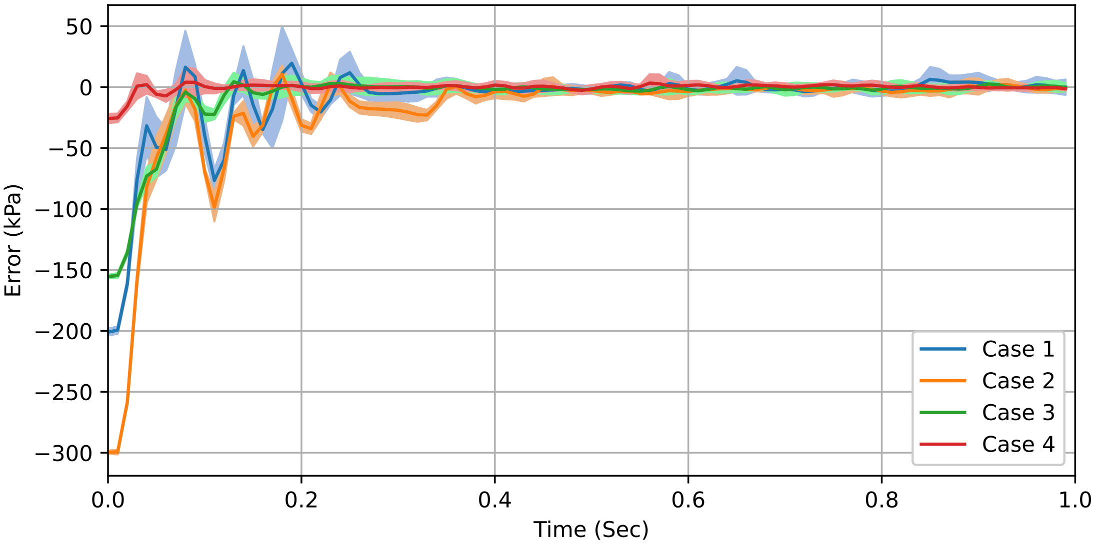

Figure 3.7: Mean and standard deviation of the pressure control's error.

Figure 3.8 presents the results of using the pressure control MPC for impedance control, and the mean and standard deviation of the error is shown in Fig. 3.9. The plot depicts that the pneumatic actuator follows the desired force output, albeit with a minor time delay of 100 ms. Table 3.4 shows the energy reuse rate and impact energy recycling rate, which are both above 80%. It is important to note that the impacts differed in each trial since they were generated manually. Despite this, the results indicate that more than 80% of the energy used to generate pneumatic springs can be reused in different parts of the system.

Detailed information regarding energy consumption and reuse rates can be found in Table 3.4. It is worth noting that the external energy inputs varied for each trial since they were performed manually. The trial with the largest external energy input was selected and is displayed in Figure 3.8 since it theoretically posed the greatest challenge for our MPC controller. The force measurement demonstrates that the output force tracks the desired force with a delay lesser than 0.05 seconds during increasing output force and less than 0.1 seconds during decreasing output force. The discrepancies at $t = 1.65$ and $t = 2.2$ are primarily due to static friction. Table 3.4 provides data on energy utilization, indicating that more than 85% of the energy used to generate resisting force can be reused for assisting. However, efficiency decreases as external impact energy increases due to heat loss proportional to the impact's speed.

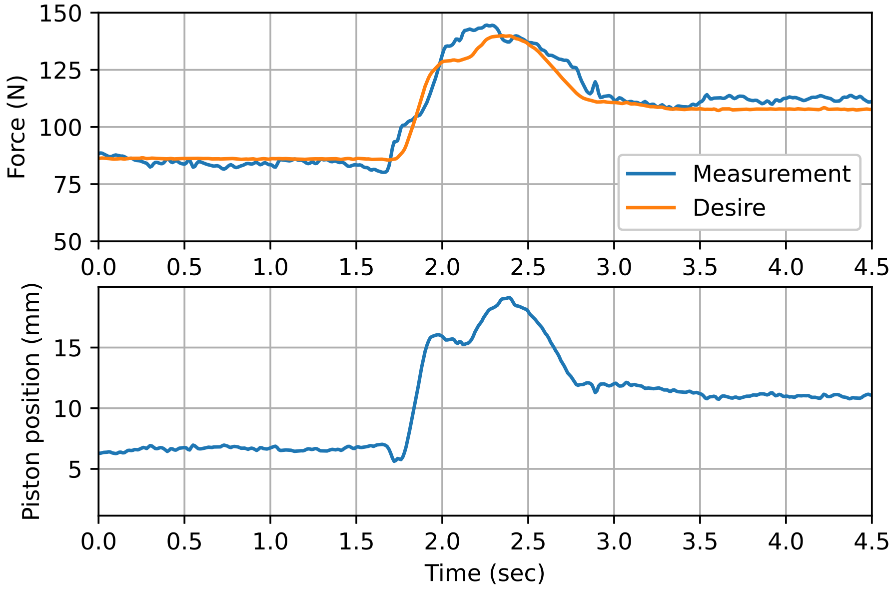

Figure 3.8: Result of impedance control. The initial force is 85N since it is pre-compressed to reach the spring's equilibrium point.

3.5 Discussion

In this study, we applied the SINDy method to learn the dynamics and delays of a system using a small sample size while avoiding overfitting. We found that our model was robust to different room temperatures, as the training data were collected at $18.33°C$ while the pressure and impedance control tests were conducted at $24°C$. It should be noted that it is

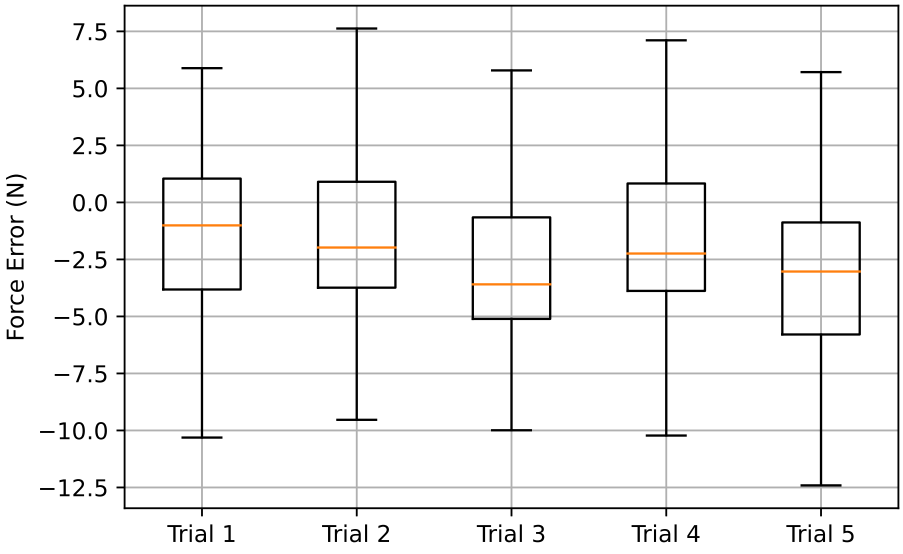

Figure 3.9: The mean and standard deviation of the error in impedance control.

the ratio, rather than the absolute difference in temperatures, that affects the flow rate.

In this study, we utilized the SINDy method to learn the dynamics and delays of a system using a small sample size while avoiding overfitting. Our findings suggest that the model we developed is robust to different room temperatures, as the training data were collected at $18.33°C$ while the pressure and impedance control tests were conducted at $24°C$. We believe it is due to the flowrate is affected by the ratio of temperatures rather than the absolute difference in temperatures, thus, $< 10°C$ has a minor effect on it. However, it was observed that the estimation of the Model Predictive Control (MPC) controller was not fully synchronized with the actual control state, as evidenced by Fig. 3.10. Despite latency introduced by computation and sensors, a relationship between latency and upper stream pressure was discovered in the estimation of the MPC controller, as shown in Fig. 3.11. Errors in the estimation increased as the upper stream pressure decreased. The researchers attributed this to the dynamic model retrieved from SINDy being more accurate at higher pressures, where energy dissipation, such as friction loss, is less significant. Despite these

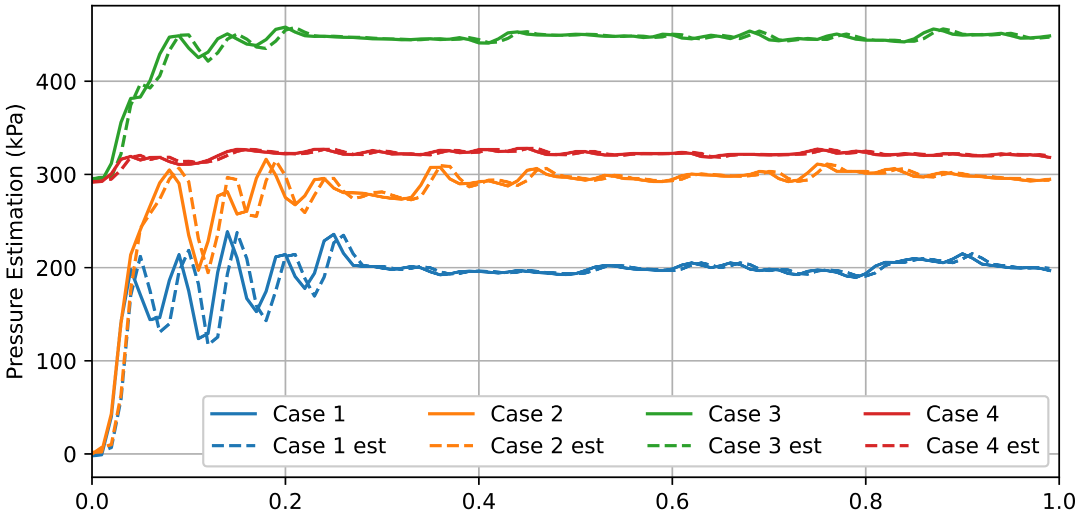

Figure 3.10: The MPC controller's estimation of the controlled state of the test scenarios in table 3.3 with the median performance (results with the median $\mathbf{R^2}$ error).

delays, the accuracy of pressure control was not negatively impacted.

Moreover, using an MPC controller resulted in a reduction in valve switching, which can extend the solenoid valves' lifespan. Fig. 3.12 depicts the valve's duty cycle for trials with the largest and smallest initial and target pressure differences. In the case of the largest pressure difference (case 2), the valve mostly operated at either 100% or 0% duty, while in the case of fine pressure tuning (case 3), the duty was nonlinearly adjusted as the cylinder's pressure approached the target value. Overall, our results suggest that the MPC controller is effective in regulating pressure and avoiding overshooting, even in the presence of latency.

The results of the impedance control experiment demonstrated that pneumatic actuators still consume energy when generating negative work. In this study, the natural pressure increment during compression was not sufficient to provide the desired impedance for the pneumatic cylinder used (6 inches stroke and 0.6 in^2 piston area). While it is possible to increase the natural pressure increment by using a cylinder with a shorter stroke or smaller piston area, this would come at the cost of reduced overall performance. For instance, using

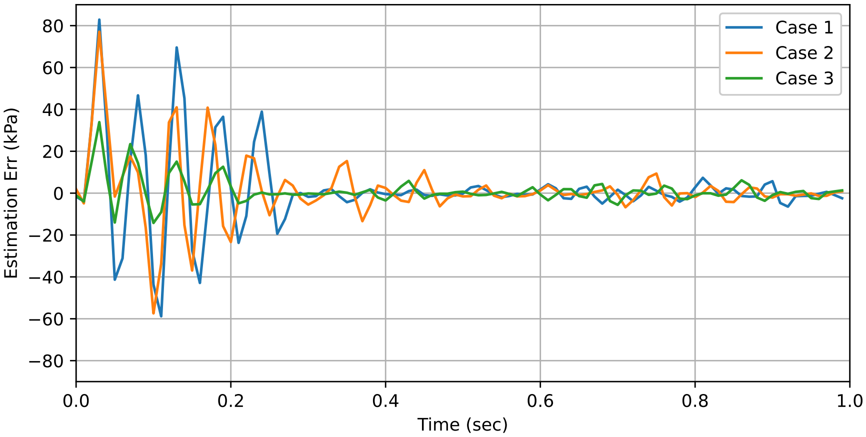

Figure 3.11: Pressure's effect on MPC controller's estimation accuracy. Both trial 1 and trial 3 increase the pressure in a similar range (200 kPa and 150 kPa), but the estimation error of the trial 3 is significantly less since the initial pressure is 300 kPa higher.

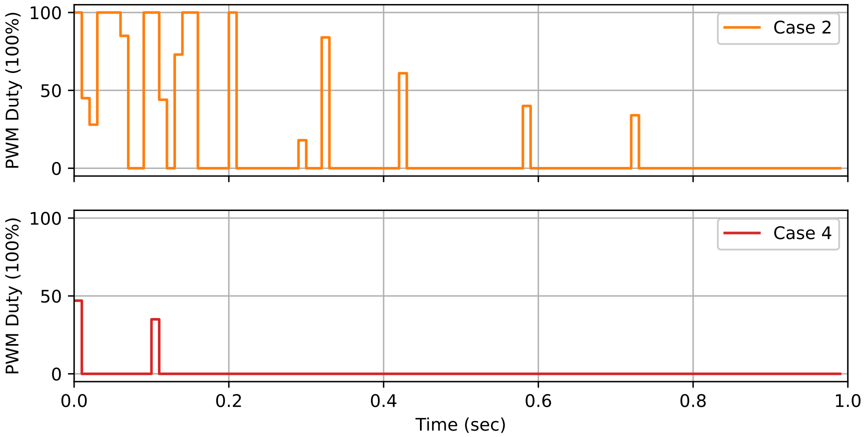

Figure 3.12: The compression of valve's PWM duty between trial 2 and trial 4, which are the trial with the largest/smallest pressure difference.

a cylinder with a shorter stroke would decrease the range of motion, while using a cylinder with a smaller piston area would require higher driving pressure, potentially damaging the solenoid valves. Nevertheless, the energy used to generate negative work can be recovered and reused for assisting. In our experiments, we found that approximately 80-90% of the energy could be recovered after the cylinder reset to its original position.

However, there are limitations to this approach of reusing energy generated by negative work in pneumatic systems. Energy can only flow from high pressure to low pressure in pneumatic systems, so the downstream side must have a lower pressure to recycle energy. This requirement can be satisfied on wearable devices if the user actively extends the downstream cylinder. However, this means that the recycled energy can only "assist" the user, rather than "driving" the user. Furthermore, the efficiency of the energy recycling process is affected by the impact energy. As the impact energy increases, there is a trend that the heat loss also increases, leading to a decrease in the rate of energy reuse. As a result, the external force only "shifts" the energy inside the cylinder to another reservoir, rather than increasing the overall energy in the system.

3.6 Conclusion

In this study, a pneumatic actuation/control scheme was presented, which utilizes low-cost solenoid valves and only-pressure measurement to achieve less than 5% error in pressure control with only increasing the pressure monotonically. The nonlinearity, latency, and unknown physical parameters of pneumatic systems were captured with ease by the sparse identification of nonlinear dynamics (SINDy) with a small sample size (around 1500 samples) but high validation/test accuracy (88.2% and 86.44%).

The proposed pneumatic actuation and control scheme is optimized for use in human performance augmenting robotics. The system provides the necessary negative work and reclaims around 88% of the energy for later assistance through the use of impedance control. As a result, it is well-suited for use in wearable devices and other robotics applications that require both negative work and energy recovery.

CHAPTER 4

Optimal Assisting Strategies for Lower-limb Exoskeleton - Device Design and Verification

4.1 Introduction

Lower limb exoskeletons designed for healthy individuals can be broadly categorized into two main groups: augmenting exoskeletons, which provide users with enhanced power capabilities, and supportive exoskeletons, which aim to reduce the user's exertion during daily tasks [97]. Representative examples of augmenting exoskeletons include those proposed by [2], [3], [98]. Devices falling into this category typically feature a comprehensive lower-body design that establishes direct contact with the ground. This design choice is necessitated by the use of robust actuators, which generate assisting forces that cannot be adequately supported by the human body and thus must be directed toward the floor. The primary objective of augmenting exoskeletons is to minimize reliance on human effort by maximizing robotic assistance. These exoskeletons typically draw energy from external sources, with limited consideration given to energy consumption efficiency. The applications of augmenting exoskeletons primarily lie within the industrial domain, such as load-carrying tasks at construction sites.

Conversely, supportive exoskeletons adopt a distinct approach as they solely aim to assist users with daily tasks. The fundamental principle underlying these devices revolves around the concept of "replacing normal human force." These designs primarily address the inefficiencies inherent in the human body's mechanical systems. Rather than constructing a separate robotic suit for assistance, the focus is on integrating additional components into the human body itself. When worn, these devices effectively substitute or assist the inefficient aspects of the human body's functionality. As their application is specific in nature, exoskeletons designed to reduce the effort required for daily tasks often prioritize characteristics such as lightweightness, compliance, and single-joint functionality. These attributes are emphasized to mitigate any discomfort that may arise for the user. While they may possess a favorable force-to-weight ratio, the power output of these supportive exoskeletons is typically limited to levels within the range of normal human capabilities. Consequently, this limitation has sparked a fundamental question within the exoskeleton community: Is it feasible to develop an augmenting exoskeleton that can efficiently provide additional power?

However, the development of an energy-efficient augmenting exoskeleton poses a fundamental challenge in the form of additional weight. Bipedal walking requires a proportional amount of energy with respect to the added weight on the limbs, and the energy consumption increases as the additional mass becomes more distal. Consequently, successful supportive exoskeletons have focused on lightweight designs that primarily augment a single joint, serving as add-ons rather than full lower-body devices. In these cases, the majority of the device's weight is borne by the user's leg during walking. However, such design concepts may not be directly applicable to augmenting exoskeletons, as they require a full lower-body configuration to effectively transfer the device's weight to the ground. Constrained by the limitations of machinable materials and existing technology, it is probable that augmenting exoskeletons will experience an inevitable increase in overall energy consumption due to the additional weight they introduce.

However, the simulation results presented in Chapter 2 shed light on a potential solution: the backward-knee configuration. Our simulations indicate that when carrying loads, a backward-knee exoskeleton that effectively harvests and reuses energy from negative and positive work can significantly reduce the *Cost of Transportation (CoT)* by up to 35%. This remarkable reduction can be attributed to two primary factors: the distinctive bending direction of the knee, which enables the user to absorb heel strikes through the knee joint, and the diminished negative work required during the swing phase, as the backward knee acts as a counterweight. Nevertheless, it is important to acknowledge the limitations of our simulation, which solely analyzed dynamics in the sagittal plane. In the three-dimensional realm, to avoid collisions between the user and the exoskeleton, the exoskeleton's legs are typically positioned to the side of the user, leading to increased inertia in the transverse plane. This limitation raises a pertinent question: Does the superiority of the backward-knee configuration persist when considering full lower-body exoskeletons in practical scenarios? In order to address this question, this chapter introduces a comprehensive lower-body exoskeleton known as PERK (Pneumatic Exoskeleton with Reversible Knee). PERK is specifically designed to optimize energy consumption during load-carrying walking tasks. The knee joint of PERK can be configured in either a forward-knee or a backward-knee configuration. To drive and recycle energy within the exoskeleton, a pneumatic actuating system is employed, utilizing the algorithm proposed in Chapter 3.

4.2 Design

The PERK (Pneumatic Exoskeleton with Reversible Knee) is a versatile exoskeleton capable of being configured into both forward-knee and backward-knee arrangements. Its primary objective is to investigate optimal methods for harnessing and reutilizing wasted energy during load-carrying human walking to provide assistance to the user. The pneumatic actuating system employed by PERK enables energy recycling and reuse across different joints. This innovative design addresses the issue of simultaneous energy loss and consumption occurring in different legs during human gait, specifically heel strikes in the leading leg and ankle push-offs in the rear leg. The selection of a pneumatic system over the more energy-efficient cable-spring transmission system was motivated by the need for precise control over impedance in various walking phases. By utilizing air as the medium, impact energy can be utilized to compress the air within the pneumatic cylinder and subsequently transmit it to other joints requiring energy input.

4.2.1 Dual Knee-directions

The PERK exoskeleton offers the flexibility to be configured in both forward-knee and backward-knee modes (see Fig. 4.1). A load, which includes the control units and the air reservoir, is attached to the upper section of the exoskeleton, securely fastened to the user's back using a backpack strap. The PERK exoskeleton encompasses six degrees of freedom (DOF), incorporating hip, knee, and ankle joints on each leg within the sagittal plane. To simplify the mechanical design, one of the joints, specifically the knee joint, is made passive as it is detached from the user. It has been observed by researchers, based on the coupling between the hip and knee joints [42], that simultaneous assistance of both the hip and knee may result in their efforts canceling each other out. In PERK, the hip joint is driven passively by the user, except during the heel strike and ankle push-off phases when it is constrained to transmit actuated forces from the knee and ankle joints to the carried load. This design allows the knee of the PERK exoskeleton to naturally bend during heel strikes, compressing the pneumatic cylinder and generating negative work while simultaneously recycling energy. The user's legs and the exoskeleton are rigidly connected at the heel using a pair of boots. This design enables the user to maintain an energy-efficient heel-sole-toe walking pattern [99].

4.2.2 Pneumatic Control

The PERK exoskeleton operates using a pneumatic driving system, comprising two identical sub-systems. The pneumatic loop within each sub-system is depicted in Fig. 4.2. An air reservoir serves as the energy source, supplying and storing pressurized air for actuation purposes. Solenoid valves are employed to regulate the pressure within each pneumatic

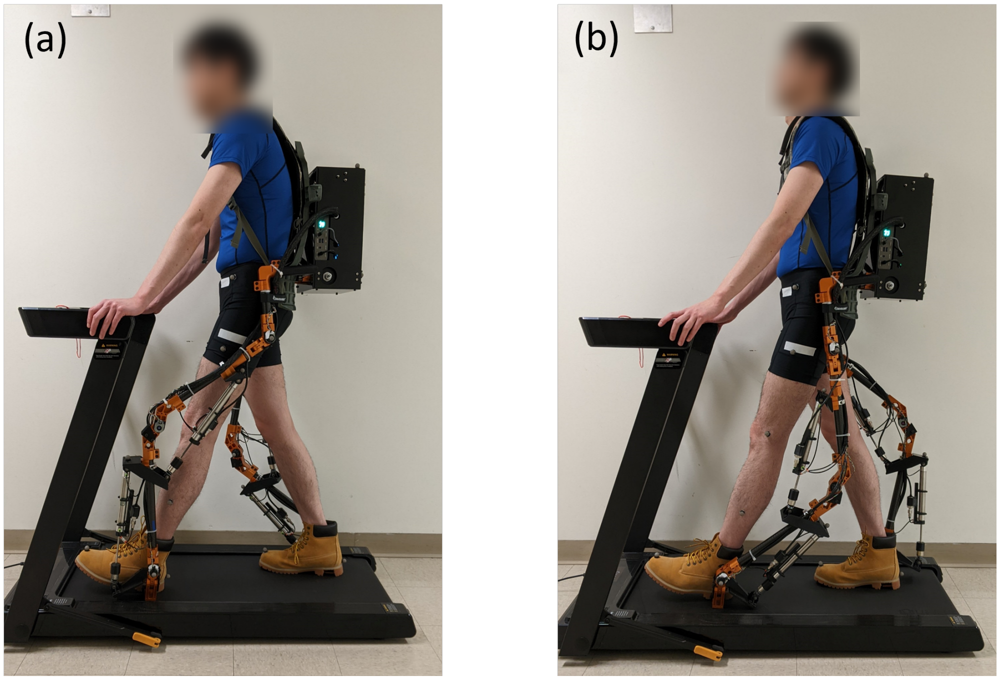

Figure 4.1: PERK in (a) forward-knee configuration. (b) backward-knee configuration.

cylinder. Pressure control for the reservoirs and pneumatic cylinders is achieved through the implementation of a model predictive controller based on Sparse Identification of Nonlinear Dynamics (SINDy), as detailed in Chapter 3.

Each individual sub-system connects the knee joint and the ankle joint on opposite legs, facilitating the direct recycling of energy lost during heel strikes for subsequent ankle push-off. The actuation sequences are illustrated in Fig. 4.3. During the initial stage of the double support phase, the pneumatic cylinder at the knee joint functions as a variable stiffness spring, generating the necessary negative work by compressing the air within the cylinder. Energy reclaimed from these pneumatic cylinders is then transmitted to the pneumatic cylinder installed on the ankle of the opposite leg. The pressure within the knee cylinder of the leading leg is regulated by an impedance controller, which generates the desired torque based on the joint angle. If the knee cylinder requires an increase in pressure, pressurized air is drawn from the reservoir. Conversely, if assistance is needed for ankle plantarflexion, pressurized air is directed towards the cylinder at the rear ankle. The desired torque for the

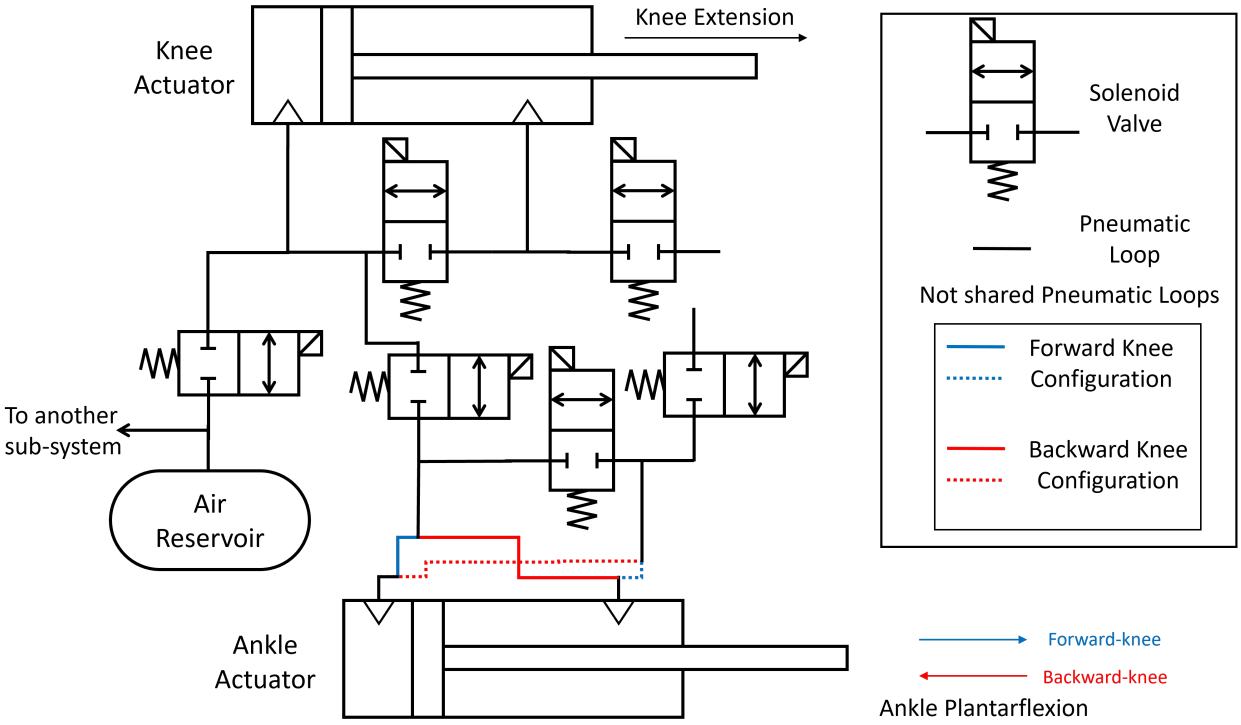

Figure 4.2: Pneumatic loops of single knee-ankle joint pair. The pneumatic cylinder at the knee joint transfers pressurized air to the opposite leg's ankle joint, converting negative work (exoskeleton's knee flexion) into positive work (exoskeleton's ankle plantarflexion).

knee joint is calculated as follows:

$$\tau_{knee} = \tau_{init} + k_{imp}(\theta - \theta_n) \tag{4.1}$$

While θ_n is the joint position when the user stands straight with PERK. τ_{init} is the torque output at θ_n, and k_{imp} is the impedance to generate the negative work.

Subsequent to the toe-off of the rear leg, the knee and ankle joints of said leg enter a state known as "free mode," wherein they operate passively and respond to the user's movements. In order to mitigate any potential resistance experienced by the user, it is imperative for the exoskeleton to minimize the torque exerted at the knee joint. In conventional exoskeleton systems, this is achieved by dissipating energy at the knee joint, thereby releasing the pressurized air contained within the chamber. However, this energy dissipation contradicts

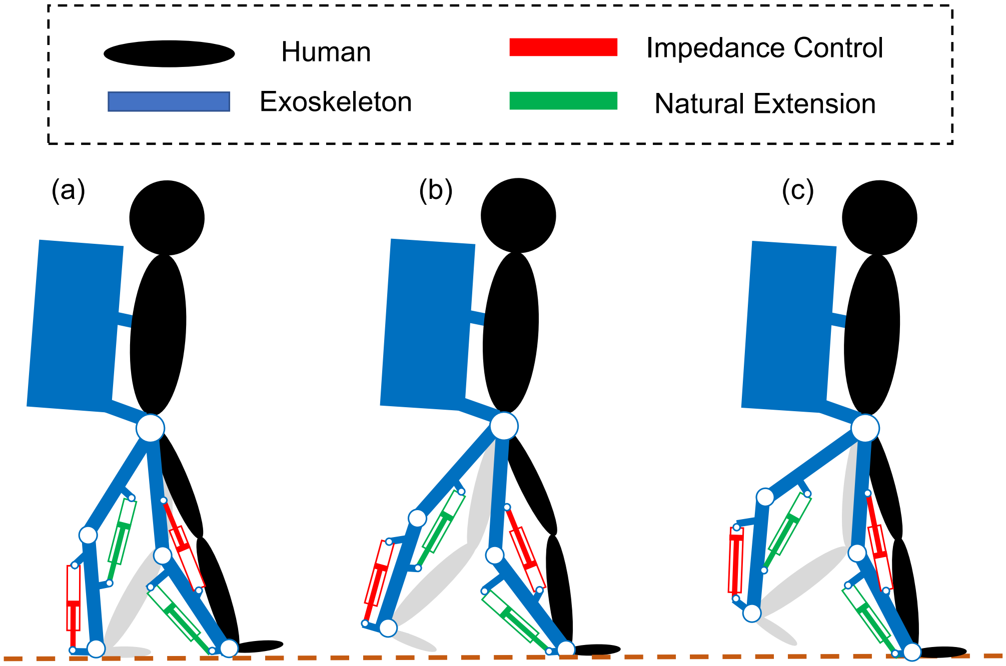

Figure 4.3: Operating principals of PERK using the backward-knee configuration as an example. (a) Beginning of double support phase. The leading knee's cylinder extends to the maximum position, and the smaller chamber of the cylinder discharges the remaining pressure, the following ankle also releases the pressurized air and provides ankle push-offs (b) During the double support phase, heel strikes occur. The leading leg's knee bends and compresses the air inside the pneumatic cylinder, the impedance of the leading is controlled by directing the pressurized air to the rear ankle to assist ankle push-off. (c) Beginning of the single support phase, toe-off occurs at the rear leg. For the swing leg, both sides of the chambers in the rear knee's cylinder are connected to allow the user to freely swing the leg.

the overarching objective of reducing energy consumption within the project. Maintaining pressurized air is crucial as the knee joint necessitates torque generation to absorb the impact during heel strike. To address this challenge, we implement regulation mechanisms for both chambers within the pneumatic cylinder, as depicted in Fig. 4.4. At the beginning of the swing phase, both chambers of the pneumatic cylinder are interconnected to minimize force output and enable unrestricted user motion. Since the outputting force is proportional to the pressure difference across the piston, it reduces the force output without any energy loss. To re-establish force output at the end of the swing phase, both chambers are disconnected and the pressurized air in one of the chambers will be discharged. Given that this operation is only required when the swinging leg is fully extended, the energy wasted in this process will be minimal.

To detect the start of the double support and single support phases, a finite state machine is employed. The state machine analyzes the angle and angular velocity of the hip joint and switches control modes accordingly.

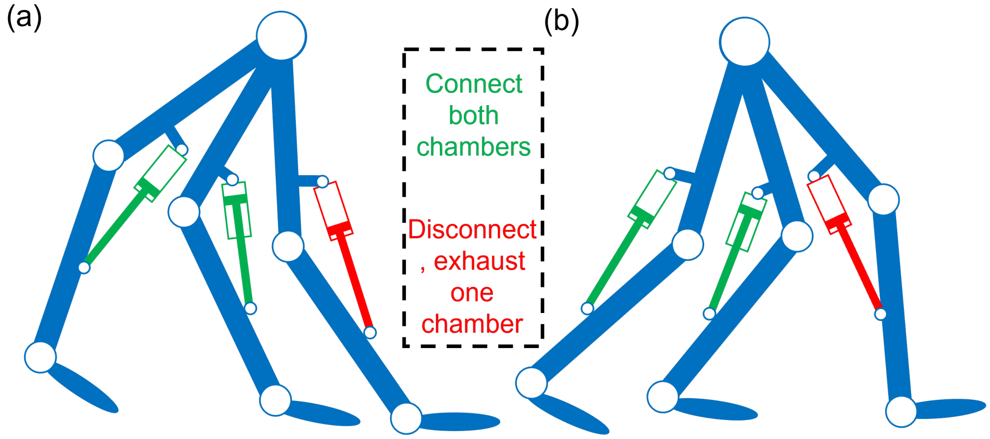

Figure 4.4: Minimal energy consumption of the knee joint for (a) backward-knee configuration and (b) forward-knee configuration. During the swing phase, the pneumatic actuator at the knee joint will balance the pressure in both chambers of the cylinder (green), and connect the smaller chamber to the atmosphere when fully extended (red). It will preserve most of the pressurized air while reducing the force output.

4.3 Experiment

To investigate the impact of different knee directions on the exoskeleton's assistive capabilities, human trials were conducted with participants walking in both forward-knee and backward-knee configurations. To simulate the effect of carrying additional loads while walking, we utilized the pneumatic valves and reservoir inside the back controller box of PERK as the representative loads. Although this may not reflect real-world scenarios, optimizing the weight of these components was beyond the scope of this research. In fact, the weight of the control/storage units was limited to commercially available products, and most of the

Table 4.1: Impedance Control Parameters Used in Different Trials

Subject #	Leg length(m)	Weight(kg)	τ_{init}(Nm)	Impedance(Nm/deg)
1	0.936	70	10	0 0.05 0.1
2	0.929	78	7	0 0.05 0.1
3	0.9659	72	8	0 0.05 0.1

parts exceeded the necessary qualifications for our study. It is important to note that the primary objective of this study is to establish a proof of concept rather than commercialize a specific device.

Table 4.1 provides the physical measurements of the test subjects involved in the experiments. Each experiment comprised two trials: one with the forward-knee configuration and another with the backward-knee configuration. At the commencement of each trial, the researcher adjusted the impedance control profile based on the user's feedback (equation 4.1). The user stood upright and wore the exoskeleton while the researcher gradually increased the assisting torque at the joints until the user perceived that the majority of the load was carried by the exoskeleton. The knee joint angle and torque measurements obtained during this phase were subsequently employed as τ_{init} and θ_n for absorbing heel strikes (equation 4.1). Given that the leg configuration is symmetric in the upright position, the same parameter values were applied to both the forward-knee and backward-knee configurations. Participants wore PERK with varying impedance profiles, as outlined in Table 4.1. The participants' movements were recorded using Vicon motion capture systems, in conjunction with the encoders and pressure sensors integrated within PERK. The captured data were subsequently processed using OpenSim [100] to obtain the inverse kinematics of the users.

4.4 Result

4.4.1 Potential Energy Exchange

During walking, users can readily perceive a noticeable difference in the effort required to swing their legs forward between the forward-knee and backward-knee configurations. This phenomenon can be explained by examining the exchange of potential energy between the human leg and the exoskeleton's leg, as illustrated in Fig. 4.5. In the forward-knee configuration, the potential energy of the human leg and the exoskeleton's leg exhibit synchronization. However, in the backward-knee configuration, this synchronization is not observed. Remarkably, during the swing phase, which starts at 50% of the gait cycle, the potential energy of the human leg becomes inversely proportional to the potential energy of the exoskeleton's leg. Consequently, the total potential energy in the backward-knee configuration remains more stable compared to the forward-knee configuration, implying reduced energy loss during each gait cycle.

4.4.2 Impulse Absorption

Figure 4.6 illustrates the energy consumption of PERK during each gait cycle for each subject. This energy consumption is defined as the difference between the total energy loss in the pneumatic system and the work output at the ankle joint during the period spanning from the heel strikes of the leading leg to the toe-off of the trailing ankle. A negative value indicates an overall increase in energy within the system. While individual users may exhibit variations in their results due to their preferred walking patterns, it is evident that the energy loss in the exoskeleton is reduced when the knees are configured in the backward direction across all tested subjects.

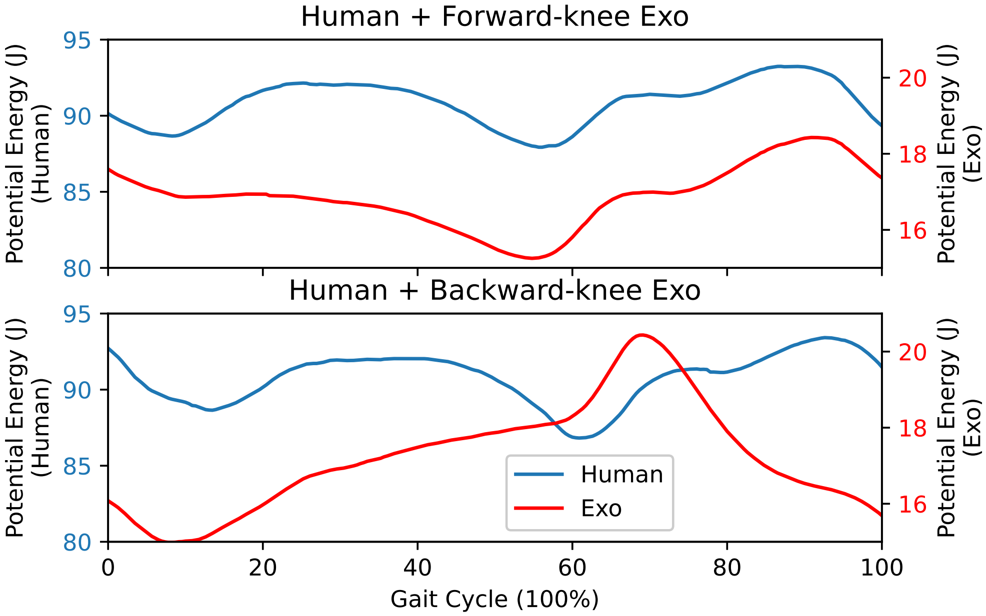

Figure 4.5: The potential energy of the user's leg and the exoskeleton's leg. The blue line is the potential energy of the human swinging leg while the red line represents the exoskeleton's swinging leg. Unlike the forward-knee configuration which both the human leg and the exoskeleton's leg share a similar profile, for the backward-knee configuration, the potential energy of the human leg and the exoskeleton's leg is sometimes inversely proportional.

4.5 Discussion

The differing potential energy profiles depicted in Figure 4.5 can be attributed to the geometric characteristics of the system. To accommodate users of varying heights, the exoskeleton's legs are designed to be longer than the user's legs, resulting in a misalignment of the center of mass between the exoskeleton's leg and the user's leg. This misalignment varies depending on the knee-bending direction. For instance, during the toe-off motion, the knee bending in the forward-knee configuration causes the exoskeleton's calf to move more upward compared to the backward-knee configuration. As a consequence of this geometric difference, the center of mass of the user wearing the backward-knee exoskeleton undergoes less vertical displacement. Given that energy losses during heel strikes redirect the center of mass from downward to upward motion, it can be anticipated that the energy loss associated

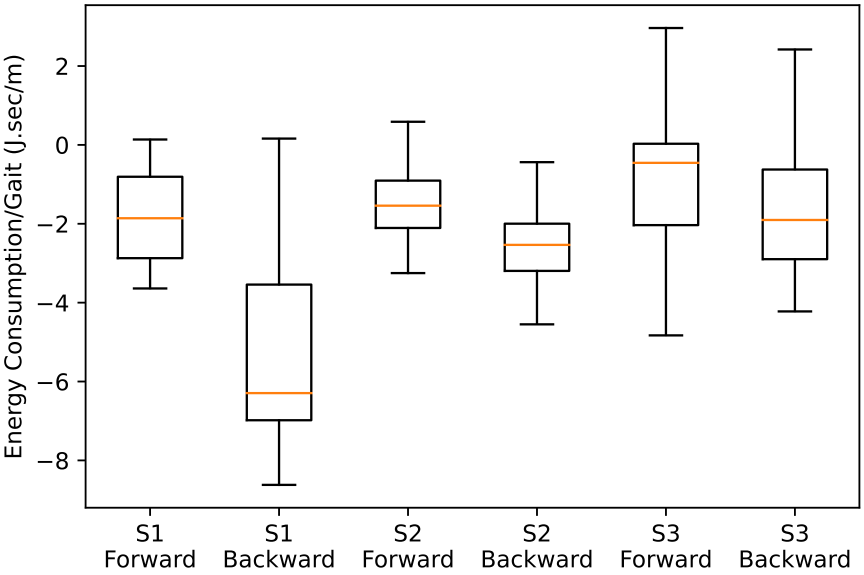

Figure 4.6: The energy loss of different test subjects per gait. A negative energy loss indicates the total energy in the system increases during the heel-strike to toe-off phase.

with wearing the backward-knee exoskeleton is lower compared to wearing the forward-knee exoskeleton.

The exoskeleton recycles the heel strikes with knee bending due to the extra leg length of the exoskeleton. However, we found it is less likely for the user's knee to flex when wearing the forward-knee exoskeleton compared to the backward-knee exoskeleton. As shown in Fig. 4.7, when configuring the exoskeleton's knee backward, the knee flexion around 5% to 15% of the gait cycle increases compared to the trajectories when wearing the forward-knee exoskeleton. This can be explained with Fig. 4.8. When attempting to recycle the impact loss with the forward-knee exoskeleton, the load will move backward, causing more interacting forces acting on the user, thus, will be avoided by the user when walking. Notably, if the user maintains a similar gait pattern while walking with both forward-knee and backward-knee configurations, the backward-knee configuration often provides greater assistance to the trailing ankle. This is depicted in Figure 4.9, which demonstrates that the energy transferred to the rear ankle for assisting ankle push-off is higher for all participants. The reason can be found in the jacobian between the vertical force at the torso and the torque at the knee joint. Fig. 4.10 is the jacobian values of different test subjects with different knee configurations. The smaller values of the backward-knee configuration indicate for the same amount of vertical impact forces, the backward-knees require higher torques. As a result, the compressed air in the knee joint's pneumatic cylinder will reach a higher pressure and will be able to drive the ankle joint with a higher force, thus, a higher output is observed.

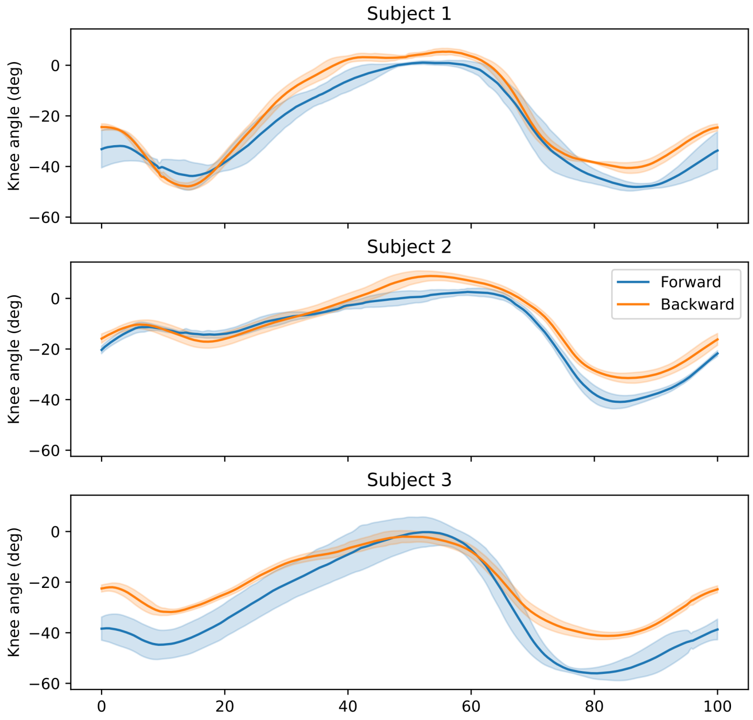

Figure 4.7: The mean/standard deviation of knee joint angles calculated with inverse kinematic from motion capture data from different test subjects while wearing the exoskeleton with different knee configurations. On average, when the exoskeleton was set to backward-knees, the users bent their knee more during the heel strike (0% to 20%). This suggests that the users use the exoskeleton to absorb the impact of the load they are carrying.

However, despite observing an increase in the total energy of the exoskeleton from heel

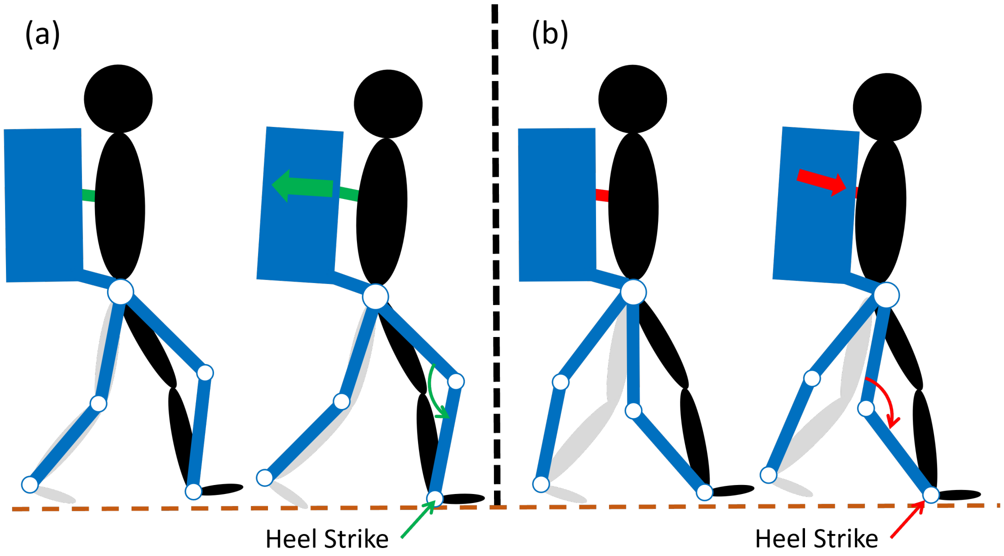

Figure 4.8: The effect of the exoskeleton's knee direction on absorbing heel strikes. When attempting to recycle the impact loss with the forward-knee exoskeleton, the load will move backward, causing more interacting forces acting on the user, thus, will be avoided by the user when walking.

strike to toe-off, it is important to note that the system lacks self-sustainability. While the current pneumatic actuating system minimizes energy loss during the swing phase with the designs in Fig. 4.4, the pneumatic cylinders do not achieve full extension at the beginning and end of this phase. Consequently, a substantial amount of energy is dissipated towards the end of the process. In addition, due to the consistently lower pressure at the ankle joint compared to the reservoir and the pneumatic cylinder at the knee joint, our current design cannot effectively harness and reuse negative work, leading to air depletion during ankle push-offs (i.e., exhaust the pressurized air that causes dorsiflexion). Addressing this limitation will require the exploration of alternative energy harvesting/reuse methods, distinct from air compression in pneumatic systems, which represents a prospective avenue for future advancements in our ongoing project.

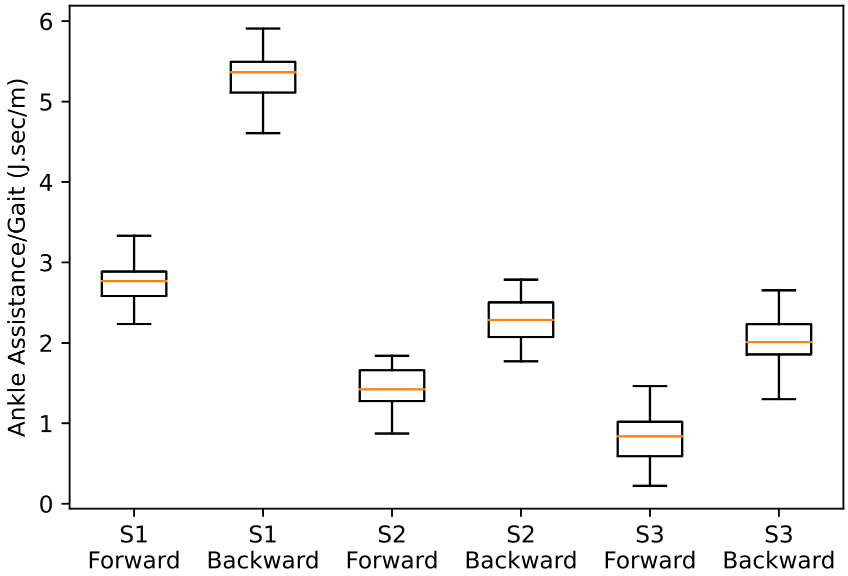

Figure 4.9: The average ankle push-off assistance per gait for different test subjects with different knee configurations. For all test subjects, the backward-knee configuration provides more assistance since the pneumatic cylinder at the knee joint is compressed to a higher pressure.

4.6 Conclusion

This chapter presented the construction of an exoskeleton that enabled the evaluation of the impact of the exoskeleton's knee direction on the user. The results demonstrated the superiority of the backward-knee exoskeleton over the forward-knee exoskeleton in both the single support (swing) phase and the double support (stand) phase. During the single support phase, the mass of the backward-knee exoskeleton acted as a counterweight, reducing the vertical displacement of the center of mass (COM) and minimizing momentum losses during heel strikes. In the double support phase, the mechanism of the backward knee facilitated enhanced energy absorption from negative work and provided greater assistance for ankle push-off. These findings highlight the benefits of the backward-knee configuration in improving the overall performance and efficiency of the exoskeleton.

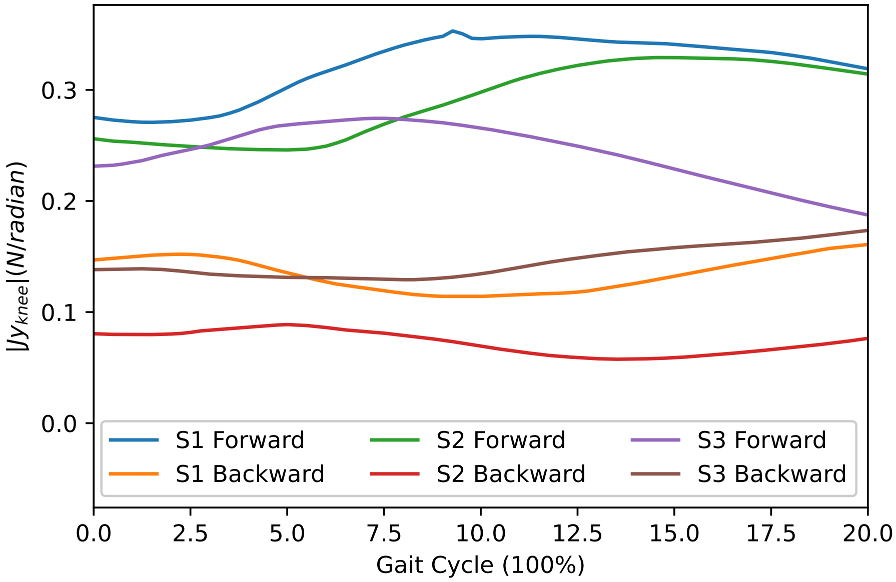

Figure 4.10: The jacobian of the vertical force and the exoskeleton's knee joint. The lower the value, the higher the pressure of the compressed air in the knee cylinders during the heel strike.

CHAPTER 5

Conclusion

This dissertation aimed to tackle the integration of conflicting exoskeleton designs, namely the augmented exoskeleton and the supportive exoskeleton. The augmented exoskeleton focuses on enhancing user performance through the provision of additional power, while the supportive exoskeleton aims to reduce energy consumption during everyday tasks. The objective was to reconcile these opposing concepts and establish a cohesive and harmonious approach. To accomplish this, a comprehensive design was undertaken for a lower-body load-carrying exoskeleton that aimed to optimize energy utilization. The research effort was divided into three distinct stages, each building upon the foundation laid by the previous stages. These stages encompassed the following: 1) Trajectory optimization was employed to determine the optimal design for the lower limb exoskeleton, 2) A pneumatic control system was developed and implemented based on the insights derived from the previous stage to deliver the desired assistance, and 3) The lower limb exoskeleton was constructed to validate the simulation results obtained.

The initial research contribution focused on optimizing assisting strategies and the mechanism through trajectory optimization. To achieve this, collision-based ground reaction forces (GRF) were incorporated into discrete Lagrangian dynamics to solve minimal-effort walking trajectories. The results revealed that the backward-knee exoskeleton demonstrated a 35% reduction in the coefficient of task (CoT) compared to normal walking, assuming efficiencies of $\mu_{resist} = 0.3$ and $_{recycle} = 0.05$. In contrast, the forward-knee exoskeleton exhibited a 15% reduction in CoT. This discrepancy can be attributed to the improved utilization of the knee joint during heel strike and the longer moment arm for the GRF during ankle push-off. Consequently, when designing an exoskeleton for load-carrying walking assistance, the backward-knee configuration is preferable. Additionally, the exoskeleton's actuators should possess the capability to recycle and reuse energy in different joints, as the ankle joint performs most of the positive work despite not collecting the highest amount of negative work.

The second research contribution involves the development of a control system capable of recycling energy from one joint and reusing it in another joint. A pneumatic actuation/control scheme was introduced in this study, utilizing low-cost solenoid valves and pressure measurements to achieve pressure control with less than 5% error while increasing pressure monotonically. The pneumatic system's nonlinearity, latency, and unknown physical parameters were effectively captured using the sparse identification of nonlinear dynamics (SINDy) with a small sample size of approximately 1500 samples. The validation and test accuracies were found to be 88.2% and 86.44%, respectively. The proposed pneumatic actuation and control scheme are optimized for applications in human performance-augmenting robotics. Through impedance control, the system provides the necessary negative work and is capable of reclaiming around 88% of the energy for later assistance. This makes it suitable for implementation in wearable devices and other robotics applications that require both negative work and energy recovery.

The final research contribution of this study involved the integration of prior knowledge to construct a full lower-body exoskeleton and validate the hypotheses. The exoskeleton, known as the Pneumatic Exoskeleton with Reversible Knees (PERK), was designed with the objective of assisting users in carrying loads while minimizing energy consumption. The results demonstrated the superiority of the backward-knee exoskeleton over the forward-knee exoskeleton in both the single support (swing) phase and the double support (stand) phase. During the single support phase, the mass of the backward-knee exoskeleton served as a counterweight, reducing the vertical displacement of the center of mass (COM) and thereby minimizing momentum losses during heel strikes. In the double support phase, the backward-knee mechanism enabled the exoskeleton to absorb more energy from negative work and provide increased assistance during ankle push-off. Considering the benefits of the backward-knee configuration in both the single-support and double-support phases, it was concluded that when energy consumption is a primary factor in designing a full lower-body exoskeleton, it is worth considering the backward-knee configuration since there is a trend that it will have less energy consumption compared to the forward-knee configuration.

Bibliography

[1] K. Yamamoto, K. Hyodo, M. Ishii, and T. Matsuo, “Development of Power Assisting Suit for Assisting Nurse Labor,” *JSME International Journal Series C Mechanical Systems, Machine Elements and Manufacturing*, vol. 45, no. 3, pp. 703–711, 2002. DOI: `10.1299/jsmec.45.703`.

[2] K. Yamamoto, M. Ishii, H. Noborisaka, and K. Hyodo, “Stand alone wearable power assisting suit - sensing and control systems,” in *RO-MAN 2004. 13th IEEE International Workshop on Robot and Human Interactive Communication (IEEE Catalog No.04TH8759)*, IEEE, 2004, pp. 661–666, ISBN: VO -. DOI: `10.1109/ROMAN.2004.1374841`.

[3] R. Steger, S. H. Kim, H. Kazerooni, and Ieee, “Control scheme and networked control architecture for the Berkeley Lower Extremity Exoskeleton (BLEEX),” in *2006 Ieee International Conference on Robotics and Automation*, 2006, pp. 3469–3476, ISBN: 0-7803-9505-0.

[4] A. B. Zoss, H. Kazerooni, and A. Chu, “Biomechanical design of the Berkeley lower extremity exoskeleton (BLEEX),” *IEEE/ASME Transactions on Mechatronics*, vol. 11, no. 2, pp. 128–138, Apr. 2006, ISSN: 1083-4435. DOI: `10.1109/TMECH.2006.871087`.

[5] G. S. Sawicki and D. P. Ferris, “Mechanics and energetics of level walking with powered ankle exoskeletons,” *Journal of Experimental Biology*, vol. 211, no. 9, pp. 1402–1413, 2008, ISSN: 0022-0949. DOI: `10.1242/jeb.009241`. [Online]. Available: `http://jeb.biologists.org/cgi/doi/10.1242/jeb.009241`.

[6] A. J. Young and D. P. Ferris, “State of the Art and Future Directions for Lower Limb Robotic Exoskeletons,” *IEEE Transactions on Neural Systems and Rehabilitation Engineering*, vol. 25, no. 2, pp. 171–182, Feb. 2017, ISSN: 1534-4320. DOI: `10.1109/TNSRE.2016.2521160`.

[7] T. F. Novacheck, “The biomechanics of running,” *Gait & Posture*, vol. 7, no. 1, pp. 77–95, Jan. 1998, ISSN: 0966-6362. DOI: `10.1016/S0966-6362(97)00038-6`. [Online]. Available: `https://www.sciencedirect.com/science/article/pii/S0966636297000386?via%7B%5C%%7D3Dihub`.

[8] R. Alo, F. Bottiglione, and G. Mantriota, “Artificial Knee Joints Actuators with Energy Recovery Capabilities: A Comparison of Performance,” *Journal of Robotics*, 2016. DOI: `10.1155/2016/4802474`. [Online]. Available: `http://downloads.hindawi.com/journals/jr/2016/4802474.pdf`.

[9] R. Chin, E. T. Hsiao-Wecksler, and E. Loth, “Fluid-Power Harvesting by Under-Foot Bellows During Human Gait,” English, *Journal of Fluids Engineering-Transactions of the Asme*, vol. 134, no. 8, p. 7, 2012. DOI: `10.1115/1.4005725`. [Online]. Available: `http://fluidsengineering.asmedigitalcollection.asme.org/pdfaccess.ashx?url=/data/journals/jfega4/926052/081101%7B%5C_%7D1.pdf`.

[10] R. Riemer and A. Shapiro, “Biomechanical energy harvesting from human motion: theory, state of the art, design guidelines, and future directions.,” *Journal of neuroengineering and rehabilitation*, vol. 8, p. 22, Apr. 2011, ISSN: 1743-0003. DOI: `10.1186/1743-0003-8-22`. [Online]. Available: `http://www.ncbi.nlm.nih.gov/pubmed/21521509%20http://www.pubmedcentral.nih.gov/articlerender.fcgi?artid=PMC3098156`.

[11] J. M. Donelan, R. Kram, and A. D. Kuo, “Mechanical work for step-to-step transitions is a major determinant of the metabolic cost of human walking,” *Journal of Experimental Biology*, vol. 205, no. 23, 3717 LP –3727, Dec. 2002. [Online]. Available: `http://jeb.biologists.org/content/205/23/3717.abstract`.

[12] N. Gurusamy, I. Elamvazuthi, N. Yahya, S. Parasuraman, and M. K. A. A. Khan, “Biomechanical energy harvesting from human lower extremity gait: A comparative

analysis," in *2017 IEEE 3rd International Symposium in Robotics and Manufacturing Automation (ROMA)*, IEEE, Sep. 2017. DOI: `10.1109/ROMA.2017.8231741`.

[13] P. Niu, P. Chapman, R. Riemer, and X. Zhang, "Evaluation of motions and actuation methods for biomechanical energy harvesting," in *2004 IEEE 35th Annual Power Electronics Specialists Conference (IEEE Cat. No.04CH37551)*, IEEE, 2004. DOI: `10.1109/pesc.2004.1355442`.

[14] M. Liu, W.-C. Tai, and L. Zuo, "Energy harvesting from ankle: Generating electricity by harvesting negative work," in *Volume 2: Mechanics and Behavior of Active Materials Structural Health Monitoring Bioinspired Smart Materials and Systems Energy Harvesting Emerging Technologies*, American Society of Mechanical Engineers, Sep. 2018. DOI: `10.1115/smasis2018-8041`.

[15] J.-P. Martin and Q. Li, "Design, model, and performance evaluation of a biomechanical energy harvesting backpack," *Mechanical Systems and Signal Processing*, vol. 134, p. 106 318, Dec. 2019. DOI: `10.1016/j.ymssp.2019.106318`.

[16] M. Cai, W.-H. Liao, and J. Cao, "A smart harvester for capturing energy from human ankle dorsiflexion with reduced user effort," *Smart Materials and Structures*, vol. 28, no. 1, p. 015 026, Dec. 2018. DOI: `10.1088/1361-665X/aaed66`.

[17] F. Gao, G. Liu, B. L.-H. Chung, H. H.-T. Chan, and W.-H. Liao, "Macro fiber composite-based energy harvester for human knee," *Applied Physics Letters*, vol. 115, no. 3, p. 033 901, Jul. 2019. DOI: `10.1063/1.5098962`.

[18] J. Fan, C.-H. Xiong, Z.-K. Huang, C.-B. Wang, and W.-B. Chen, "A lightweight biomechanical energy harvester with high power density and low metabolic cost," *Energy Conversion and Management*, vol. 195, pp. 641–649, Sep. 2019. DOI: `10.1016/j.enconman.2019.05.025`.

[19] H. Shi, Y. Yue, H. Wang, J. Xu, and X. Mei, "Design and performance analysis of human walking induced energy recovery system by means of hydraulic energy

conversion and storage," *Energy Conversion and Management*, vol. 217, p. 113 008, Aug. 2020. DOI: `10.1016/j.enconman.2020.113008`.

[20] K. E. Zelik and A. D. Kuo, "Human walking isn't all hard work: Evidence of soft tissue contributions to energy dissipation and return," *Journal of Experimental Biology*, vol. 213, no. 24, pp. 4257–4264, Dec. 2010. DOI: `10.1242/jeb.044297`.

[21] P. Malcolm, W. Derave, S. Galle, and D. D. Clercq, "A simple exoskeleton that assists plantarflexion can reduce the metabolic cost of human walking," *PLoS ONE*, vol. 8, no. 2, C. M. Aegerter, Ed., e56137, Feb. 2013. DOI: `10.1371/journal.pone.0056137`.

[22] S. Galle, P. Malcolm, W. Derave, and D. D. Clercq, "Enhancing performance during inclined loaded walking with a powered ankle–foot exoskeleton," *European Journal of Applied Physiology*, vol. 114, no. 11, pp. 2341–2351, Jul. 2014. DOI: `10.1007/s00421-014-2955-1`.

[23] Y. Ding, F. A. Panizzolo, C. Siviy, *et al.*, "Effect of timing of hip extension assistance during loaded walking with a soft exosuit," *Journal of NeuroEngineering and Rehabilitation*, vol. 13, no. 1, Oct. 2016. DOI: `10.1186/s12984-016-0196-8`.

[24] S. Galle, P. Malcolm, S. H. Collins, and D. D. Clercq, "Reducing the metabolic cost of walking with an ankle exoskeleton: Interaction between actuation timing and power," *Journal of NeuroEngineering and Rehabilitation*, vol. 14, no. 1, Apr. 2017. DOI: `10.1186/s12984-017-0235-0`.

[25] S. H. Collins, M. B. Wiggin, and G. S. Sawicki, "Reducing the energy cost of human walking using an unpowered exoskeleton," *Nature*, vol. 522, no. 7555, pp. 212–215, Apr. 2015. DOI: `10.1038/nature14288`.

[26] S. Lee, S. Crea, P. Malcolm, I. Galiana, A. Asbeck, and C. Walsh, "Controlling negative and positive power at the ankle with a soft exosuit," in *2016 IEEE International Conference on Robotics and Automation (ICRA)*, IEEE, May 2016, pp. 3509–3515. DOI: `10.1109/ICRA.2016.7487531`.

[27] L. Xie, G. Huang, L. Huang, S. Cai, and X. Li, “An unpowered flexible lower limb exoskeleton: Walking assisting and energy harvesting,” *IEEE/ASME Transactions on Mechatronics*, vol. 24, no. 5, pp. 2236–2247, Oct. 2019. DOI: `10.1109/TMECH.2019.2933983`.

[28] R. C. BROWNING, J. R. MODICA, R. KRAM, and A. GOSWAMI, “The effects of adding mass to the legs on the energetics and biomechanics of walking,” *Medicine &amp Science in Sports &amp Exercise*, vol. 39, no. 3, pp. 515–525, Mar. 2007. DOI: `10.1249/mss.0b013e31802b3562`.

[29] L. M. Mooney, E. J. Rouse, and H. M. Herr, “Autonomous exoskeleton reduces metabolic cost of human walking during load carriage,” *Journal of NeuroEngineering and Rehabilitation*, vol. 11, no. 1, May 2014. DOI: `10.1186/1743-0003-11-80`.

[30] G. S. Sawicki, C. L. Lewis, and D. P. Ferris, “It pays to have a spring in your step,” *Exercise and Sport Sciences Reviews*, vol. 37, no. 3, pp. 130–138, Jul. 2009. DOI: `10.1097/JES.0b013e31819c2df6`.

[31] J. T. Webber and D. A. Raichlen, “The role of plantigrady and heel-strike in the mechanics and energetics of human walking with implications for the evolution of the human foot,” *Journal of Experimental Biology*, vol. 219, no. 23, pp. 3729–3737, Dec. 2016. DOI: `10.1242/jeb.138610`.

[32] G. A. Cavagna, N. C. Heglund, and C. R. Taylor, “Mechanical work in terrestrial locomotion: Two basic mechanisms for minimizing energy expenditure,” *American Journal of Physiology-Regulatory, Integrative and Comparative Physiology*, vol. 233, no. 5, R243–R261, Nov. 1977. DOI: `10.1152/ajpregu.1977.233.5.R243`.

[33] D. J. Farris and G. S. Sawicki, “The mechanics and energetics of human walking and running: A joint level perspective,” *Journal of The Royal Society Interface*, vol. 9, no. 66, pp. 110–118, May 2011. DOI: `10.1098/rsif.2011.0182`.

[34] T. K. Uchida, J. L. Hicks, C. L. Dembia, and S. L. Delp, “Stretching your energetic budget: How tendon compliance affects the metabolic cost of running,” *PLOS ONE*, vol. 11, no. 3, A. A. Zadpoor, Ed., e0150378, Mar. 2016. DOI: `10.1371/journal.pone.0150378`.

[35] A. G. Schache, Y. C. Lin, K. M. Crossley, and M. G. Pandy, “Is running better than walking for reducing hip joint loads?” *Medicine and Science in Sports and Exercise*, vol. 50, no. 11, pp. 2301–2310, Nov. 2018. DOI: `10.1249/MSS.0000000000001689`.

[36] J. Rubenson, D. G. Lloyd, D. B. Heliams, T. F. Besier, and P. A. Fournier, “Adaptations for economical bipedal running: The effect of limb structure on three-dimensional joint mechanics,” *Journal of The Royal Society Interface*, vol. 8, no. 58, pp. 740–755, Oct. 2010. DOI: `10.1098/rsif.2010.0466`.

[37] J. W. Rankin, J. Rubenson, and J. R. Hutchinson, “Inferring muscle functional roles of the ostrich pelvic limb during walking and running using computer optimization,” *Journal of The Royal Society Interface*, vol. 13, no. 118, p. 20 160 035, May 2016. DOI: `10.1098/rsif.2016.0035`.

[38] M. Haberland and S. Kim, “On extracting design principles from biology: II. case study—the effect of knee direction on bipedal robot running efficiency,” *Bioinspiration &amp Biomimetics*, vol. 10, no. 1, p. 016 011, Feb. 2015. DOI: `10.1088/1748-3190/10/1/016011`.

[39] R. L. Marsh, D. J. Ellerby, H. T. Henry, and J. Rubenson, “The energetic costs of trunk and distal-limb loading during walking and running in guinea fowlinumida meleagris/i,” *Journal of Experimental Biology*, vol. 209, no. 11, pp. 2050–2063, Jun. 2006. DOI: `10.1242/jeb.02226`.

[40] T. W. FLYNN, S. M. CONNERY, M. A. SMUTOK, R. J. ZEBALLOS, and I. M. WEISMAN, “Comparison of cardiopulmonary responses to forward and backward

walking and running," *Medicine &amp Science in Sports &amp Exercise*, vol. 26, no. 1, 89???94, Jan. 1994. DOI: `10.1249/00005768-199401000-00015`.

[41] J. E. Bertram and A. Gutmann, "Motions of the running horse and cheetah revisited: Fundamental mechanics of the transverse and rotary gallop," *Journal of The Royal Society Interface*, vol. 6, no. 35, pp. 549–559, Oct. 2008. DOI: `10.1098/rsif.2008.0328`.

[42] C. L. Dembia, A. Silder, T. K. Uchida, J. L. Hicks, and S. L. Delp, "Simulating ideal assistive devices to reduce the metabolic cost of walking with heavy loads," *PLOS ONE*, vol. 12, no. 7, Ø. Sandbakk, Ed., e0180320, Jul. 2017. DOI: `10.1371/journal.pone.0180320`.

[43] J.-t. Zhang and Q. Li, "Investigation of a passive inter-limb device on step-to-step transition of human walking," in *2013 IEEE 13th International Conference on Rehabilitation Robotics (ICORR)*, 2013, pp. 1–5. DOI: `10.1109/ICORR.2013.6650434`.

[44] J. T. Betts, *Practical Methods for Optimal Control Using Nonlinear Programming, Third Edition*. Society for Industrial and Applied Mathematics, Jan. 2020. DOI: `doi:10.1137/1.9781611976199`.

[45] M. Kelly, "An introduction to trajectory optimization: How to do your own direct collocation," *SIAM Review*, vol. 59, no. 4, pp. 849–904, Jan. 2017. DOI: `10.1137/16m1062569`.

[46] K. Mombaur, "Using optimization to create self-stable human-like running," *Robotica*, vol. 27, no. 3, pp. 321–330, May 2009. DOI: `10.1017/S0263574708004724`.

[47] G. Schultz and K. Mombaur, "Modeling and optimal control of human-like running," *IEEE/ASME Transactions on Mechatronics*, vol. 15, no. 5, pp. 783–792, Oct. 2010. DOI: `10.1109/TMECH.2009.2035112`.

[48] E. C. Kuska, J. A. Barrios, and A. L. Kinney, "Multi-segment foot model reveals distal joint kinematic differences between habitual heel-toe walking and non-habitual toe walking," *Journal of Biomechanics*, vol. 110, p. 109 960, Sep. 2020. DOI: `10.1016/j.jbiomech.2020.109960`.

[49] I. Mordatch, E. Todorov, and Z. Popović, "Discovery of complex behaviors through contact-invariant optimization," *ACM Transactions on Graphics*, vol. 31, no. 4, pp. 1–8, Aug. 2012. DOI: `10.1145/2185520.2185539`.

[50] Y. Gonthier, J. McPhee, C. Lange, and J.-C. Piedbœuf, "A contact modeling method based on volumetric properties," in *Volume 6: 5th International Conference on Multibody Systems, Nonlinear Dynamics, and Control, Parts A, B, and C*, ASMEDC, Jan. 2005. DOI: `10.1115/DETC2005-84610`.

[51] M. Peasgood, E. Kubica, and J. McPhee, "Stabilization of a dynamic walking gait simulation," *Journal of Computational and Nonlinear Dynamics*, vol. 2, no. 1, pp. 65–72, Jul. 2006. DOI: `10.1115/1.2389230`.

[52] M. Ezati, P. Brown, B. Ghannadi, and J. McPhee, "Comparison of direct collocation optimal control to trajectory optimization for parameter identification of an ellipsoidal foot–ground contact model," *Multibody System Dynamics*, vol. 49, no. 1, pp. 71–93, Mar. 2020. DOI: `10.1007/s11044-020-09731-3`.

[53] Z. Manchester, N. Doshi, R. J. Wood, and S. Kuindersma, "Contact-implicit trajectory optimization using variational integrators," *The International Journal of Robotics Research*, vol. 38, no. 12-13, pp. 1463–1476, May 2019. DOI: `10.1177/0278364919849235`.

[54] D. A. Winter, *Biomechanics and Motor Control of Human Movement.* John Wiley & Sons, Inc., Sep. 2009. DOI: `10.1002/9780470549148`.

[55] E. M. Arnold, S. R. Ward, R. L. Lieber, and S. L. Delp, "A model of the lower limb for analysis of human movement," *Annals of Biomedical Engineering*, vol. 38, no. 2, pp. 269–279, Dec. 2009. DOI: `10.1007/s10439-009-9852-5`.

[56] S. Jahn, J. Seror, and J. Klein, “Lubrication of articular cartilage,” *Annual Review of Biomedical Engineering*, vol. 18, no. 1, pp. 235–258, Jul. 2016. DOI: `10.1146/annurev-bioeng-081514-123305`.

[57] J. Taborri, E. Palermo, S. Rossi, and P. Cappa, “Gait partitioning methods: A systematic review,” *Sensors*, vol. 16, no. 1, p. 66, Jan. 2016. DOI: `10.3390/s16010066`.

[58] R. A. Brand, “The biomechanics and motor control of human gait: Normal, elderly, and pathological,” *Journal of Biomechanics*, vol. 25, no. 8, p. 949, Aug. 1992. DOI: `10.1016/0021-9290(92)90236-T`.

[59] B. Vanderborght, B. Verrelst, R. V. Ham, *et al.*, “Exploiting natural dynamics to reduce energy consumption by controlling the compliance of soft actuators,” *The International Journal of Robotics Research*, vol. 25, no. 4, pp. 343–358, Apr. 2006. DOI: `10.1177/0278364906064566`.

[60] L. Miskovic, M. Dezman, and T. Petric, “Pneumatic quasi-passive variable stiffness mechanism for energy storage applications,” *IEEE Robotics and Automation Letters*, vol. 7, no. 2, pp. 1705–1712, Apr. 2022. DOI: `10.1109/LRA.2022.3141211`.

[61] K. Anam and A. A. Al-Jumaily, “Active exoskeleton control systems: State of the art,” *Procedia Engineering*, vol. 41, pp. 988–994, 2012. DOI: `10.1016/j.proeng.2012.07.273`.

[62] Y. Sun, P. Tang, D. Dong, J. Zheng, X. Chen, and L. Bai, “Modeling and experimental evaluation of a pneumatic variable stiffness actuator,” *IEEE/ASME Transactions on Mechatronics*, pp. 1–12, 2021. DOI: `10.1109/TMECH.2021.3116871`.

[63] N. Herzig, R. Moreau, A. Leleve, and M. T. Pham, “Stiffness control of pneumatic actuators to simulate human tissues behavior on medical haptic simulators,” in *2016 IEEE International Conference on Advanced Intelligent Mechatronics (AIM)*, IEEE, Jul. 2016. DOI: `10.1109/AIM.2016.7576997`.

[64] J. Bobrow and B. McDonell, “Modeling, identification, and control of a pneumatically actuated, force controllable robot,” *IEEE Transactions on Robotics and Automation*, vol. 14, no. 5, pp. 732–742, 1998. DOI: `10.1109/70.720349`.

[65] D. Aoyagi, W. Ichinose, S. Harkema, D. Reinkensmeyer, and J. Bobrow, “An assistive robotic device that can synchronize to the pelvic motion during human gait training,” in *9th International Conference on Rehabilitation Robotics, 2005. ICORR 2005.*, IEEE, 2005, pp. 565–568. DOI: `10.1109/ICORR.2005.1502026`.

[66] S.-H. Hyon, T. Hayashi, A. Yagi, T. Noda, and J. Morimoto, “Design of hybrid drive exoskeleton robot XoR2,” in *2013 IEEE/RSJ International Conference on Intelligent Robots and Systems*, IEEE, Nov. 2013. DOI: `10.1109/iros.2013.6697024`.

[67] J. Meuleman, E. van Asseldonk, G. van Oort, H. Rietman, and H. van der Kooij, “LOPES II—design and evaluation of an admittance controlled gait training robot with shadow-leg approach,” *IEEE Transactions on Neural Systems and Rehabilitation Engineering*, vol. 24, no. 3, pp. 352–363, Mar. 2016. DOI: `10.1109/TNSRE.2015.2511448`.

[68] K. E. Gordon and D. P. Ferris, “Learning to walk with a robotic ankle exoskeleton,” *Journal of Biomechanics*, vol. 40, no. 12, pp. 2636–2644, Jan. 2007. DOI: `10.1016/j.jbiomech.2006.12.006`.

[69] S. Hussain, S. Q. Xie, and P. K. Jamwal, “Adaptive impedance control of a robotic orthosis for gait rehabilitation,” *IEEE Transactions on Cybernetics*, vol. 43, no. 3, pp. 1025–1034, Jun. 2013. DOI: `10.1109/TSMCB.2012.2222374`.

[70] S. M. Mirvakili and I. W. Hunter, “Artificial muscles: Mechanisms, applications, and challenges,” *Advanced Materials*, vol. 30, no. 6, p. 1 704 407, Dec. 2017. DOI: `10.1002/adma.201704407`.

[71] D. Saravanakumar, B. Mohan, and T. Muthuramalingam, "A review on recent research trends in servo pneumatic positioning systems," *Precision Engineering*, vol. 49, pp. 481–492, Jul. 2017. DOI: `10.1016/j.precisioneng.2017.01.014`.

[72] H.-P. Ren, J.-T. Fan, and O. Kaynak, "Optimal design of a fractional-order proportional-integer-differential controller for a pneumatic position servo system," *IEEE Transactions on Industrial Electronics*, vol. 66, no. 8, pp. 6220–6229, Aug. 2019. DOI: `10.1109/TIE.2018.2870412`.

[73] X. Shen and M. Goldfarb, "Independent stiffness and force control of pneumatic actuators for contact stability during robot manipulation," in *Proceedings of the 2005 IEEE International Conference on Robotics and Automation*, IEEE, 2005. DOI: `10.1109/robot.2005.1570521`.

[74] Festo. [Online]. Available: `https://www.festo.com/`.

[75] Z. Li, Y. Wang, H. Du, and Z. Hu, "Modelling and analysis of full-vehicle hydro-pneumatic suspension system considering real-gas polytropic process," *Mechanical Systems and Signal Processing*, vol. 165, p. 108 406, Feb. 2022. DOI: `10.1016/j.ymssp.2021.108406`.

[76] N. Ye, S. Scavarda, M. Betemps, and A. Jutard, "Models of a pneumatic PWM solenoid valve for engineering applications," *Journal of Dynamic Systems, Measurement, and Control*, vol. 114, no. 4, pp. 680–688, Dec. 1992. DOI: `10.1115/1.2897741`.

[77] D. Ben-Dov and S. Salcudean, "A force-controlled pneumatic actuator," *IEEE Transactions on Robotics and Automation*, vol. 11, no. 6, pp. 906–911, 1995. DOI: `10.1109/70.478438`.

[78] A. Messina, N. I. Giannoccaro, and A. Gentile, "Experimenting and modelling the dynamics of pneumatic actuators controlled by the pulse width modulation (PWM) technique," *Mechatronics*, vol. 15, no. 7, pp. 859–881, Sep. 2005. DOI: `10.1016/j.mechatronics.2005.01.003`.

[79] R. van Varseveld and G. Bone, "Accurate position control of a pneumatic actuator using on/off solenoid valves," *IEEE/ASME Transactions on Mechatronics*, vol. 2, no. 3, pp. 195–204, 1997. DOI: `10.1109/3516.622972`.

[80] H. Langjord, T. A. Johansen, and C. Bratli, "Dual-mode switched control of an electropneumatic clutch actuator with input restrictions," in *2009 European Control Conference (ECC)*, IEEE, Aug. 2009. DOI: `10.23919/ECC.2009.7074712`.

[81] B. Hejrati and F. Najafi, "Accurate pressure control of a pneumatic actuator with a novel pulse width modulation sliding mode controller using a fast switching on/off valve," *Proceedings of the Institution of Mechanical Engineers, Part I: Journal of Systems and Control Engineering*, vol. 227, no. 2, pp. 230–242, Nov. 2012. DOI: `10.1177/0959651812459303`.

[82] T. Nguyen, J. Leavitt, F. Jabbari, and J. E. Bobrow, "Accurate sliding-mode control of pneumatic systems using low-cost solenoid valves," *IEEE/ASME Transactions on Mechatronics*, vol. 12, no. 2, pp. 216–219, Apr. 2007. DOI: `10.1109/TMECH.2007.892821`.

[83] G. Andrikopoulos, G. Nikolakopoulos, and S. Manesis, "Pneumatic artificial muscles: A switching model predictive control approach," *Control Engineering Practice*, vol. 21, no. 12, pp. 1653–1664, Dec. 2013. DOI: `10.1016/j.conengprac.2013.09.003`.

[84] E. Richer and Y. Hurmuzlu, "A high performance pneumatic force actuator system: Part i—nonlinear mathematical model," *Journal of Dynamic Systems, Measurement, and Control*, vol. 122, no. 3, pp. 416–425, Jun. 1999. DOI: `10.1115/1.1286336`.

[85] R. Zhang, J. Peng, H. Li, *et al.*, "A predictive control method to improve pressure tracking precision and reduce valve switching for pneumatic brake systems," *IET Control Theory & Applications*, vol. 15, no. 10, pp. 1389–1403, Mar. 2021. DOI: `10.1049/cth2.12130`.

[86] L. G. Vailati and M. Goldfarb, "A method for mass flow and displacement estimation in a pneumatic actuation system using valve-based pressure sensing," *IEEE/ASME Transactions on Mechatronics*, pp. 1–1, 2020. DOI: `10.1109/TMECH.2020.3011348`.

[87] S. L. Brunton, J. L. Proctor, and J. N. Kutz, "Discovering governing equations from data by sparse identification of nonlinear dynamical systems," *Proceedings of the National Academy of Sciences*, vol. 113, no. 15, pp. 3932–3937, Mar. 2016. DOI: `10.1073/pnas.1517384113`.

[88] S. E. Askarinejad, A. Fahim, M. R. H. Yazdi, and M. T. Masouleh, "Data-driven identification of the jacobian matrix of a 2- DoF spherical parallel manipulator," in *2019 7th International Conference on Robotics and Mechatronics (ICRoM)*, IEEE, Nov. 2019. DOI: `10.1109/ICRoM48714.2019.9071873`.

[89] E. Kaiser, J. N. Kutz, and S. L. Brunton, "Sparse identification of nonlinear dynamics for model predictive control in the low-data limit," *Proceedings of the Royal Society A: Mathematical, Physical and Engineering Sciences*, vol. 474, no. 2219, p. 20 180 335, Nov. 2018. DOI: `10.1098/rspa.2018.0335`.

[90] G. Mamakoukas, M. L. Castano, X. Tan, and T. D. Murphey, "Derivative-based koopman operators for real-time control of robotic systems," *IEEE Transactions on Robotics*, vol. 37, no. 6, pp. 2173–2192, Dec. 2021. DOI: `10.1109/TRO.2021.3076581`.

[91] U. Fasel, J. N. Kutz, B. W. Brunton, and S. L. Brunton, "Ensemble-SINDy: Robust sparse model discovery in the low-data, high-noise limit, with active learning and control," *Proceedings of the Royal Society A: Mathematical, Physical and Engineering Sciences*, vol. 478, no. 2260, Apr. 2022. DOI: `10.1098/rspa.2021.0904`.

[92] H. Lee and J. Rosen, "Lower limb exoskeleton - energy optimization of bipedal walking with energy recycling - modeling and simulation," *IEEE Robotics and Automation Letters*, pp. 1–8, 2023. DOI: `10.1109/lra.2023.3234813`.

[93] T. J. Roberts and N. Konow, "How tendons buffer energy dissipation by muscle," *Exercise and Sport Sciences Reviews*, vol. 41, no. 4, pp. 186–193, Oct. 2013. DOI: `10.1097/JES.0b013e3182a4e6d5`.

[94] T. Wang, Y. Zhang, Z. Chen, and S. Zhu, "Parameter identification and model-based nonlinear robust control of fluidic soft bending actuators," *IEEE/ASME Transactions on Mechatronics*, vol. 24, no. 3, pp. 1346–1355, Jun. 2019. DOI: `10.1109/TMECH.2019.2909099`.

[95] G. Granosik and J. Borenstein, "Minimizing air consumption of pneumatic actuators in mobile robots," in *IEEE International Conference on Robotics and Automation, 2004. Proceedings. ICRA '04. 2004*, IEEE, 2004. DOI: `10.1109/ROBOT.2004.1308820`.

[96] B. Stellato, G. Banjac, P. Goulart, A. Bemporad, and S. Boyd, "OSQP: An operator splitting solver for quadratic programs," *Mathematical Programming Computation*, vol. 12, no. 4, pp. 637–672, 2020. DOI: `10.1007/s12532-020-00179-2`. [Online]. Available: `https://doi.org/10.1007/s12532-020-00179-2`.

[97] H. Lee, P. W. Ferguson, and J. Rosen, "Lower limb exoskeleton systems—overview," pp. 207–229, 2020. DOI: `10.1016/B978-0-12-814659-0.00011-4`.

[98] M. Fontana, R. Vertechy, S. Marcheschi, F. Salsedo, and M. Bergamasco, "The body extender: A full-body exoskeleton for the transport and handling of heavy loads," *IEEE Robotics &amp Automation Magazine*, vol. 21, no. 4, pp. 34–44, Dec. 2014. DOI: `10.1109/MRA.2014.2360287`.

[99] J. R. Usherwood, A. J. Channon, J. P. Myatt, J. W. Rankin, and T. Y. Hubel, "The human foot and heel–sole–toe walking strategy: A mechanism enabling an inverted pendular gait with low isometric muscle force?" *Journal of The Royal Society Interface*, vol. 9, no. 75, pp. 2396–2402, May 2012. DOI: `10.1098/rsif.2012.0179`.

[100] S. L. Delp, F. C. Anderson, A. S. Arnold, *et al.*, "OpenSim: Open-source software to create and analyze dynamic simulations of movement," *IEEE Transactions on*

Biomedical Engineering, vol. 54, no. 11, pp. 1940–1950, Nov. 2007. DOI: `10.1109/TBME.2007.901024`.